Current Research in Toxicology 8 (2025) 100212

Contents lists available at ScienceDirect

Current Research in Toxicology

journal homepage: www.journals.elsevier.com/current-research-in-toxicology

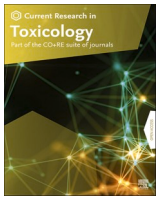

Research Paper

The role of the gut microbiota and the nicotinate/nicotinamide pathway in rotenone-induced neurotoxicity

Yan Sai *, Wei Ge, Li Zhong, Qifu Zhang, Jingsong Xiao, Yaohui Shan, Wenqi Ye, Haoyin Liu, Shulin Liu, Feng Ye, Xiaogang Wang, He Tang, Yuanpeng Zhao, Guorong Dan

Institute of Toxicology, College of Preventive Medicine, Army Medical University, Chongqing 400038, China

ARTICLE INFO

Keywords:
Rotenone
Neurotoxicity
Gut microbiota
Metabolomics
Inflammatory response
Nicotinate and nicotinamide metabolic pathways

ABSTRACT

Rotenone is a natural compound from plants. It is widely used in pesticides because of highly toxic to insects and fish. However, lots of research has reported that rotenone has neurotoxic effects in humans. It is confirmed there is a correlation between rotenone exposure and Parkinson's disease (PD). Therefore, the role of gut microbiota and related metabolic pathways was investigated in rotenone-induced neurotoxicity. The results showed that the abundance of gut microbiota changed significantly. The differential metabolites were enriched in the nicotinate and nicotinamide metabolism pathways, which had the greatest impact on the entire metabolic system. The contents of acetic acid and butyric acid in intestinal tissues decreased significantly. Additionally, Interleukin-6 (IL-6), Tumor necrosis factor alpha (TNF-α) and vasoactive intestinal peptide (VIP) were significantly up-regulated, while gastrin (GAS) and Ghrelin were significantly down-regulated. Expression of intestinal tight junction protein was significantly reduced. Moreover, nicotinamide adenine dinucleotide (NAD^+), a the product of the nicotinate/nicotinamide pathways, decreased significantly. And the expression levels of nicotinamide phosphoribosyl transferase (NAMPT) and Solute Carrier Family 25 Member 51 (SLC25A51) also reduced significantly. Therefore, gut microbiota was influenced obviously in rats exposed to rotenone, leading to a decrease of acetic acid and butyric acid contents, which might in turn affect the change of intestinal barrier permeability and induce inflammatory reactions. Meanwhile, the nicotinate/nicotinamide metabolic pathways might play an important role in rats exposed to rotenone.

Introduction

Rotenone is a natural compound extracted from the roots of subtropical leguminous Derris and many other plants. It has been regarded as a safe and effective insecticide and has been widely used for the treatment of agricultural pests (Greenamyre et al., 2000; Tanner et al., 2011). At the same time, the high toxicity of rotenone to humans and livestock has also attracted extensive notice. Since 2000, rotenone has attracted much attention when the major features of PD-like could be reproduced in rats infused with rotenone (Betarbet et al., 2000). Subsequently, a large number of epidemiological data and laboratory studies have shown a correlation between rotenone exposure and the onset of sporadic PD. It is known that rotenone is an inhibitor of the mitochondrial complex I and can lead to the damage of the oxidative phosphorylation system (OXPHOS) (Ibarra-Gutiérrez et al., 2023). Rotenone has a strong lipophilicity and can penetrate the blood–brain barrier and cell membrane, resulting in neurodegeneration and the development of PD-like symptoms (Coulom and Birman, 2004; Di Monte, 2003; Guo et al., 2022). PD is the world's second largest neurodegenerative disease after Alzheimer's disease. Its pathogenesis is very complex, which may involve neuroinflammation, oxidative stress, mitochondrial dysfunction, and so on (Morris et al., 2024).

In the living environment, the human body is colonized by microorganisms, most of which are located in the gastrointestinal tract, forming a unique gut microbiota (GM). The research on GM has found that it maintains dynamic equilibrium with the host under normal conditions and plays an important role in various metabolic processes (Milani et al., 2017). GM can digest food to provide nutrition and promote the human immune system to form a natural barrier (Adak and Khan, 2019). The disorder of GM is related to many diseases (Zmora

* Corresponding author.
E-mail addresses: sai2000cn@163.com (Y. Sai), gewei1020@qq.com (W. Ge), 415377127@qq.com (L. Zhong), zqf5022@163.com (Q. Zhang), xiaoxinli7318@163.com (J. Xiao), syh1529632904@163.com (Y. Shan), 422742604@qq.com (W. Ye), 1124832787@qq.com (H. Liu), 1020454093@qq.com (S. Liu), 293312620@qq.com (F. Ye), xiaogangwang@tmmu.edu.cn (X. Wang), 466174@qq.com (H. Tang), zhaopolly@qq.com (Y. Zhao), liroy@163.com (G. Dan).

https://doi.org/10.1016/j.crtox.2024.100212
Received 29 October 2024; Received in revised form 11 December 2024; Accepted 16 December 2024
Available online 24 December 2024

et al., 2019). Moreover, the clinical presentation of the PD include motor delay, muscle rigidity, static tremors, anxiety, cognitive impairment, insomnia, etc. Related studies have shown that when the gut microbiota of PD patients was transplanted into mice, the fecal microbiota of PD patients significantly damaged motor function compared to the microbiota of the healthy control group (Sampson et al., 2016). In another study, PD patients have improved motor and non-motor symptoms after receiving fecal microbiota transplantation treatment (Xue et al., 2020). The results indicate that GM may play a key and functional role in the pathogenesis of PD. Therefore, in the present study, we explored the role of GM in rotenone-induced neurotoxicity.

Here, animal model of rotenone-induced neurotoxicity was established, and the samples of rat feces, intestines, and striatal tissues were used for metabonomics detection and conjoint analysis. Through metabolomics techniquests, our study aims to explore the complex interplay between gut microbiota and the metabolic pathways, which could potentially open new avenues for therapeutic interventions and a deeper understanding of the pathophysiology of rotenone-induced neurodegeneration and also to provide ideas for the prevention and treatment of PD.

Materials and methods

Animals

The animal experiments were conducted in accordance with the National Institutes of Health Guide for the Care and Use of Laboratory. Animals were approved by the Animal Care Committee of the Army Medical University. The male Wister rats (200–250 g) were purchased from the Animal Laboratory Center of Army Medical University (Chongqing, China). The rats were housed in a special pathogen-free (SPF) environment of the animal feeding chamber with free access to diet and water, a 12 h light/dark cycle, a temperature of 23 ± 2 °C, and a humidity of 45 ± 5 %. After 1 week of acclimatization in the animal feeding chamber, all rats were randomly divided into two groups (N = 20 for each group): control group and rotenone exposure group. According to the method of establishing an early rotenone-induced PD rat model, the three-stage model was established by subcutaneous injection of rotenone solution (Sigma, St Louis, MO, USA). The doses were 2.0 mg/kg for 3 days, 1.0 mg/kg for 7 days, 0.5 mg/kg for 20 days, once a day for 30 days (Peng et al., 2018; Xiao et al., 2023; Zhang et al., 2017). Rotenone powder was dissolved in DMOS solution (Sigma, St Louis, MO, USA) and then diluted to corresponding concentrations with normal saline for injection. At the same time, the control group were subcutaneously injected with the same amount of DMSO solution and saline injection daily, for 30 consecutive days. After 30 days of intervention, all rats were carried on with behavioral test.

Behavioral tests

The rats were placed in an open-field reaction box with video recording, which was 40 cm in height and 100 cm in length at the bottom. The inner wall was covered with black cloth, and the bottom was divided into 25 squares of 4 cm × 4 cm on average. A camera was set 2 m directly above, and the vision could cover the whole interior of the open field. During the experiment, the experimenters and computers and other equipment were placed in another room to reduce the disturbance to the animals, and the laboratory background noise was controlled in a quiet environment below 65 dB. Recording stopped after 5 min. Then, the total distance, average speed, and number of entries into the central area were recorded by using a motion tracking system. After each rat was tested, 75 % alcohol was used to clean the inner wall and the bottom of the box to avoid the residual urine or odour from the previous rat affecting the next test results. Subsequently, the animals were replaced and the experiments were continued (Kraeuter et al., 2019; Prut and Belzung, 2003).

Sample selection

Rats were anesthetized intraperitoneally with 20 % urethane at a dose of 7 mL/kg. Blood was collected. The serum was separated by centrifugation at 4000 rpm. At a distance of 10 cm from the ileocecal junction, the distal ileum tissues with a length of more than 1 cm were cut off and rinsed. The head of the rat was cut off and the striatum was quickly dissected according to the anatomy of rat brain. After collection, transfer each sample to −80 °C for storage.

Cecal index

After abdominal anesthesia in rats, the body mass of rats was weighed and the abdominal cavity was opened. The ileocecal portion of the intestine was located, both ends of the cecum were ligated, and the cecum was cut and weighed. The cecal index was recorded and calculated. The specific formula is: cecal index = cecal mass/rat weight.

Metabonomics detection and analysis

The cryopreserved tissues (−80 °C, n = 6/group) were sent to Biotree Biomedical Science and Technology Co., Ltd. (Shanghai, China) for metabonomics detection and the detection results were analyzed.

Intestinal microbiota testing

The total genomic DNA of the stool samples was extracted from the samples by the CTAB/SDS method. The concentration and purity of DNA were detected on 1 % agarose gel. According to different concentrations, DNA was diluted to 1 ng/μL with sterile water. The V3-V4 region of the bacterial 16S rRNA gene was amplified by using specific primers. PCRs were carried out using 15 μL of Phusion® High-Fidelity PCR Master Mix (New England Biolabs, USA), 0.2 mM of forward and reverse primers, and approximately 10 ng of template DNA. The PCR products were electrophoresed on a 2 % agarose gel and were purified using a gel extraction kit (Qiagen, Germany). Finally, high-throughput sequencing was performed on the Illumina Nova Seq 6000 platform.

The Uparse software (Uparse v7.0.1001, https://drive5.com/uparse/) was employed to cluster the data of all samples. Sequence clustering was transformed into operational taxonomic units (OTUs) with 97 % identity. Subsequently, species annotation was performed by comparing with the known microbial 16S rRNA database. Then, the changes in species diversity and abundance of the samples were analyzed to investigate the differences and community compositions of dominant species in different samples. Moreover, species with significant differences at each level were screened.

Short-chain fatty acid targeting metabolomics with gas chromatography-mass spectrometry (GC–MS)

The samples of the intestinal and striatal tissues were placed in the EP tubes and extracted with 1 mL H_2O, mixing for 10 s with vortex. Then steel balls were added and the samples were homogenized in ball mill for 4 min at 40 Hz. Then it was treated with ultrasound for 5 min (incubated in ice water), repeating for 3 times. Then the samples were incubated for 2 h at −40 °C and centrifuged at 5000 rpm at 4 °C for 20 min, and the supernatant was extracted into a new EP tube. 100 μL of 50 % H_2SO_4 and 800 μL of extracting solution (25 mg/L stock in methyl *tert*-butyl ether) were added as internal standard. The mixtures were vortexed for 10 s. Subsequently the samples were centrifuged at 4 °C for 15 min and the supernatant was removed. Then the samples were detected by GC–MS. The SHIMADZU GC2030-QP2020 NX gas chromatography-mass spectrometer was used to detect the samples. The system utilized a HP-FFAP capillary column. 1 μL aliquot of the analyte was injected in split mode (5:1). Helium was used as the carrier gas, the front inlet purge flow was 3 mL/min, and the gas flow rate through the column was 1 mL/min. The initial temperature was kept at 80 °C for 1 min. Thereafter, it was elevated to 200 °C at a rate of 10 °C/min and remained at this

temperature for 5 min. Subsequently, it was raised to 240 °C at a rate of 40 °C/min and maintained at this temperature for 1 min. The temperatures of injection, transfer line, quad, and ion source were respectively set to 240 °C, 240 °C, 150 °C, and 200 °C. The mass spectrometry data were acquired in Scan/SIM mode with the *m/z* range of 33–150 after a solvent delay of 3.5 min.

Non-target metabolomics of rat feces with ultra high performance liquid chromatography-Q exactive orbitrap-mass spectrometry (UHPLC-QE-MS)

Animal tissues were cleaned in the same method, and 500 μL of extract solution (methanol: acetonitrile: water = 2:2:1, with isotopically-labelled internal standard mixture) were added. After homogenization, the samples were incubated for 1 h at −40 °C and were centrifuged at 12,000 rpm for 15 min at 4 °C. The resulting supernatant was transferred into a fresh glass vial for analysis. LC-MS/MS analyses were carried out using an UHPLC system (Vanquish, Thermo Fisher Scientific), which was coupled with a UPLC BEH Amide column (2.1 mm × 100 mm, 1.7 μm) and a Q Exactive HFX mass spectrometer (Orbitrap MS, Thermo). The LC phase A was aqueous, containing 25 mmol/L ammonium acetate and 25 mmol/L ammonia, and phase B was acetonitrile. Sample disk temperature: 4 °C, injection volume: 2 μL. The QE HFX mass spectrometer was employed to acquire MS/MS spectra in information-dependent acquisition (IDA) mode, which was under the control of the acquisition software (Xcalibur, Thermo). The acquisition software continuously evaluated the full scan MS spectrum. The electrospray ionization (ESI) source conditions were configured as follows: sheath gas flow rate was set to 30 Arb; Aux gas flow rate was 25 Arb; capillary temperature was maintained at 350 °C; full MS resolution was set at 120000; MS/MS resolution was 7500; collision energy was 10/30/60 in normalized collision energy (NCE) mode; and spray voltage was 3.6 kV (positive) or −3.2 kV (negative), respectively.

The raw data were converted to the mzXML format using ProteoWizard and were processed with an in-house program, which was developed using R and based on XCMS, for peak detection, extraction, alignment, and integration. Then an in-house MS2 database (BiotreeDB) was applied in metabolite annotation. The cutoff for annotation was set at 0.3.

600 MRM high-throughput targeting metabolomics

Animal tissues were cleaned in the same method, and 200 μL of H_2O and 800 μL of extraction solution (methanol:acetonitrile = 1:1, containing isotope internal standard) were added. After the samples were homogenized and centrifuged, the resulting supernatants were transferred to several new EP tubes and then condensed to dryness by centrifugation. 160 μL of 60 % acetonitrile was added for full dissolution. The samples were centrifuged for 15 min at 12000 rpm, then the supernatant was removed and detected.

The target compounds were separated chromatographically by employing an H-Class (Waters) ultra-high performance liquid chromatograph in a Waters Atlantis Premier BEH Z-HILIC Column (1.7 μm, 2.1 mm * 150 mm). Mobile phase A was ultrapure water and acetonitrile in a ratio of 8:2, containing 10 mmol/L ammonium acetate. Mobile phase B was acetonitrile and ultrapure water in a ratio of 9:1, also containing 10 mmol/L ammonium acetate. Both mobile phases A and B were adjusted to pH 9 using ammonia water. The temperature of the sample tray was 8 °C. The injection volume was 1 μL. Finally, a SCIEX 6500 QTRAP + triple quadrupole mass spectrometer equipped with an IonDrive Turbo V ESI ion source was used for mass spectrometry analysis in multiple reaction monitoring (MRM) mode. The ion source parameters were as follows: Curtain Gas = 35 psi, IonSpray Voltage = +5000 V/−4500 V, Temperature = 400 °C, Ion Source Gas 1 = 50 psi, Ion Source Gas 2 = 50 psi. A series of preparation and organization (data management) on the raw data were performed, filtering individual metabolites and only retaining metabolite data with single group empty values of no more than 50 % or all group empty values of no more than 50 %. Simulate missing values in the original data. The numerical simulation method involves filling in the minimum value by multiplying it by a random number between (0.1, 0.5).

Enzyme-linked immunosorbent assay (ELISA)

After the samples were homogenized and centrifuged, the supernatant was removed for detection. The serum was detected directly by ELISA. The ELISA detection kits were equilibrated at room temperature for 30 min before use. According to the method described in the instruction manual, 50 μL of standards were added and the samples were tested respectively. At the same time, 100 μL of detection antibody labeled with horseradish peroxidase (HRP) was added, respectively. Incubation was carried out at 37 °C in the dark for 60 min. After washing five times, 100 μL of substrate mixture was added. Continue to incubate at 37 °C in the dark for 15 min. Finally, 50 μL of termination solution was added into all wells and the absorbance of each well was read at a wavelength of 450 nm on a microplate reader. A standard curve was drawn and the content of corresponding factors in each group of samples was calculated. The ELISA detection kits are as follows: Interleukin-6 (#RX302856R, RUIXIN Biotech, China), Tumor necrosis factor alpha (#RX302058R, RUIXIN Biotech, China), vasoactive intestinal peptide (#RX302215R, RUIXIN Biotech, China), Gastrin (#RX302271R, RUIXIN Biotech, China), Ghrelin (#RX301269R, RUIXIN Biotech, China).

Intestinal histological examination with HE staining and transmission electron microscopy techniques

The intestinal tissues were fully fixed with 4 % paraformaldehyde (#P0099, Beyotime, Shanghai, China) and were dehydrated in gradient alcohol. And then the dehydrated tissues were subjected to transparency treatment followed by wax immersion, embedding, trimming, slicing, and sticking steps. The slices were deparaffinized, rehydrated, and stained with hematoxylin eosin using xylene. The stained slices were sealed with neutral gum and observed. A digital medical image acquisition and processing system was used to capture images, and morphological indicators such as villus height and crypt depth of the ileal mucosa were observed.

After being fixed on filter paper, the samples were trimmed to a size of approximately 2 mm × 2 mm using a blade. And then they were immediately placed into electron microscope fixative (#G1102, Servicebio, China). The tissues were fixed at room temperature for 2 h and then transferred for storage at 4 °C. Finally, transmission electron microscopy was employed to observe the ultrastructural changes of intestinal tissues.

Western blotting

The lysates of the intestinal and striatal tissues were prepared according to the standard method. The BCA protein quantification kit (#P0009, Beyotime, Shanghai, China) was utilized to detect the protein concentration of the lysate. Load 100 μg of protein per well onto a 10 % SDS-PAGE gel for animal tissues. Subsequently, the protein was transferred into a polyvinylidene fluoride (PVDF) membrane (#ISEQ00010, Merck millipore, Germany). Then it was blocked with 5 % skim milk at room temperature for 2 h and incubated with different primary antibodies overnight at 4 °C. After incubation, it was washed for three times with TBST. And then it was incubated with anti-rabbit IgG secondary antibody at room temperature for 100 min. Finally, the expression band of the target protein was detected by the enhanced chemiluminescence detection kit (Beyotime, Shanghai, China), and the expression intensity of the target protein was analyzed by ImageJ software. Antibody and dilutions were as follows: β-actin (#AC026, rabbit, 1:50,000; ABclonal, Wuhan, China), NAMPT (#11776-1-AP, rabbit, 1:1000; Proteintech, Wuhan, China), SLC25A51 (#A21105, rabbit, 1:1000; ABclonal, Wuhan, China), Occludin (#13409-1-AP, rabbit, 1:5000; Proteintech, Wuhan, China), Claudin 1 (#13050-1-AP, rabbit, 1:1000; Proteintech,

Wuhan, China), ZO-1(#21773-1-AP, rabbit, 1:5000; Proteintech, Wuhan, China).

Detection of NAD$^+$/NADH content

According to the manufacturer's instructions, NAD$^+$/NADH extraction solution was added and the operation was performed on ice. Subsequently, the samples were centrifuged at 12,000 × g and 4 °C for 10 min. The separated supernatant was taken as the sample to be tested. NADH standard was used as the reference, and then the samples were measured with the NAD$^+$/NADH detection kit (#S0175, Beyotime, Shanghai, China) and the quantities of NAD$^+$, NADH, and NAD total were calculated.

Statistical analysis

Data were analyzed using GraphPad Prism version 8.0.2 (Graph Pad Software, USA) and SPSS 20.0. Statistical significances between the two groups were tested by a two-tailed, unpaired Student's *t*-test. A one-way analysis of variance (ANOVA) followed by Tukey's multiple comparisons test was used for more than two groups. Results were presented as the mean ± standard error of the mean (SEM). A significance threshold of $P < 0.05$ was established. The asterisk in all figures indicated significant differences between the control groups and the rotenone exposure groups (*$P < 0.05$, **$P < 0.01$, ***$P < 0.001$).

Results

Effects of rotenone on general symptoms and behavioral tests in rats

The rats of the control group were active, with shiny hair and a good mental state. However the apparent physical signs were induced by rotenone. With the rotenone exposure, the fur of the rats gradually turned dark yellow, and their feces appeared loose and fluffy. The rats also showed reduced autonomous activity and characteristics similar to PD syndrome. Some rats also experienced typical tense clonic seizures, including seizures of the forelimbs, head and face muscles, systemic muscle tension, crawling, vertical tail sign, and shortness of breath.

Using the open field test, the total distance, average speed, and number of entries into the central area were analyzed. Compared with the control group, rats exposed to rotenone had significantly reduced total distance, average speed, and number of entries into the central area

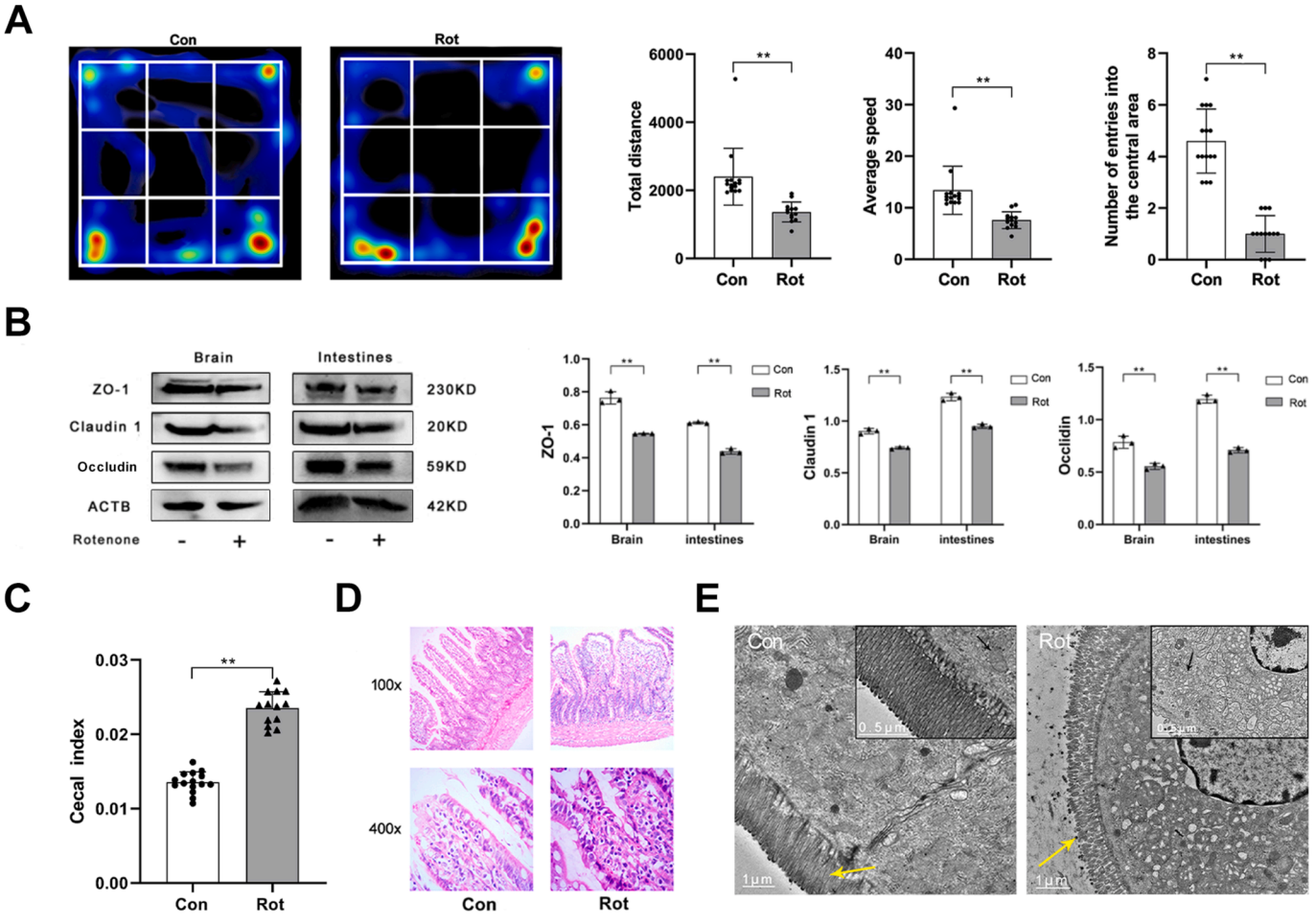

Fig. 1. Alterations in neurobehavior, cecal index, pathological structure of intestinal tissue and tight junction proteins on the rat model of PD-like induced by rotenone. (A) The moving trail of rats was recorded in the open field test. The results showed the total distance, average speed, and number of entries into the central area. Con: control group, Rot: rotenone exposure group. The values represent the means ± SEM. **: $P < 0.01$, compared with control group. (B) Expression of tight junction proteins (ZO-1, Claudin 1, and Occludin) in intestinal and brain tissues. ACTB is used as a loading control. The values represent the means ± SEM. **: $P < 0.01$, compared with control group. (C) Comparison of cecal index between control group and poisoned group. Cecal index = cecal mass/animal weight. The values represent the means ± SEM. **: $P < 0.01$, compared with control group. (D) HE staining of rat intestinal tissue. Observe under 100× and 400× light mirror fields respectively. (E) Transmission electron microscopy of rat intestinal tissues. The yellow arrow indicates the position of intestinal villi, and the black arrow indicates the position of mitochondria. (For interpretation of the references to color in this figure legend, the reader is referred to the web version of this article.)

($P < 0.01$) (Fig. 1A). The results indicated that the motor function and exploratory desire of rats exposed to rotenone were significantly weakened.

Effects of rotenone on the expression of intestinal tight junction protein (ZO-1, Occuldin, Claudin-1) in rats

The blood–brain barrier and intestinal barrier are special physiological barriers, which have the functions of regulating material exchange and maintaining the homeostasis, protecting the body from endogenous microorganisms and their toxins. The expression of tight junction proteins ZO-1, Claudin 1 and Occludin was observed in intestinal and brain tissues of rats respectively. The results showed that rotenone exposure significantly reduced the expression of tight junction proteins in the intestinal and brain tissues compared with the control group ($P < 0.01$) (Fig. 1B). In the intestinal tissues, ZO-1, Claudin 1 and Occludin decreased by an average of approximately 28 %, 23 % and 41 % respectively; in the brain tissues, ZO-1, Claudin 1 and Occludin decreased by an average of approximately 28 %, 18 % and 29 % respectively. These results further confirmed that rotenone could disrupt the function of intestinal barrier and blood–brain barrier, aggravating the influence of harmful factors on the body.

Effects of rotenone on cecal index and the pathological structure and mitochondrial morphology of intestinal tissues in rats

Compared with the normal group, the cecum of rats treated with rotenone was significantly enlarged, with an increase in water content. And the cecum index was significantly higher than that of the control group. The cecal tissues of rats exposed to rotenone were transparent and were filled with gas, with an increased in volume. When the cecal was cut, a large amount of thin material could be seen flowing out. After calculation, the cecal index of rats exposed to rotenone significantly increased ($P < 0.01$) (Fig. 1C).

According to the intestinal HE staining results (Fig. 1D), the control group of rats had intact intestinal mucosal epithelium, neatly arranged glands, and scattered goblet cells with abundant villi protruding into the intestinal cavity. A small amount of inflammatory cells was scattered in the submucosal layer. The intestinal mucosa of rats treated with rotenone showed significant thinning, with partial shedding of epithelium, deep staining of mucosal cell cytoplasm, reduction of goblet cells, shortening of villi, and mild interstitial congestion. There was a significant difference compared to the control group.

In further study, electron microscopy was used to observe the structure of small intestinal villi (Fig. 1E). The results of transmission

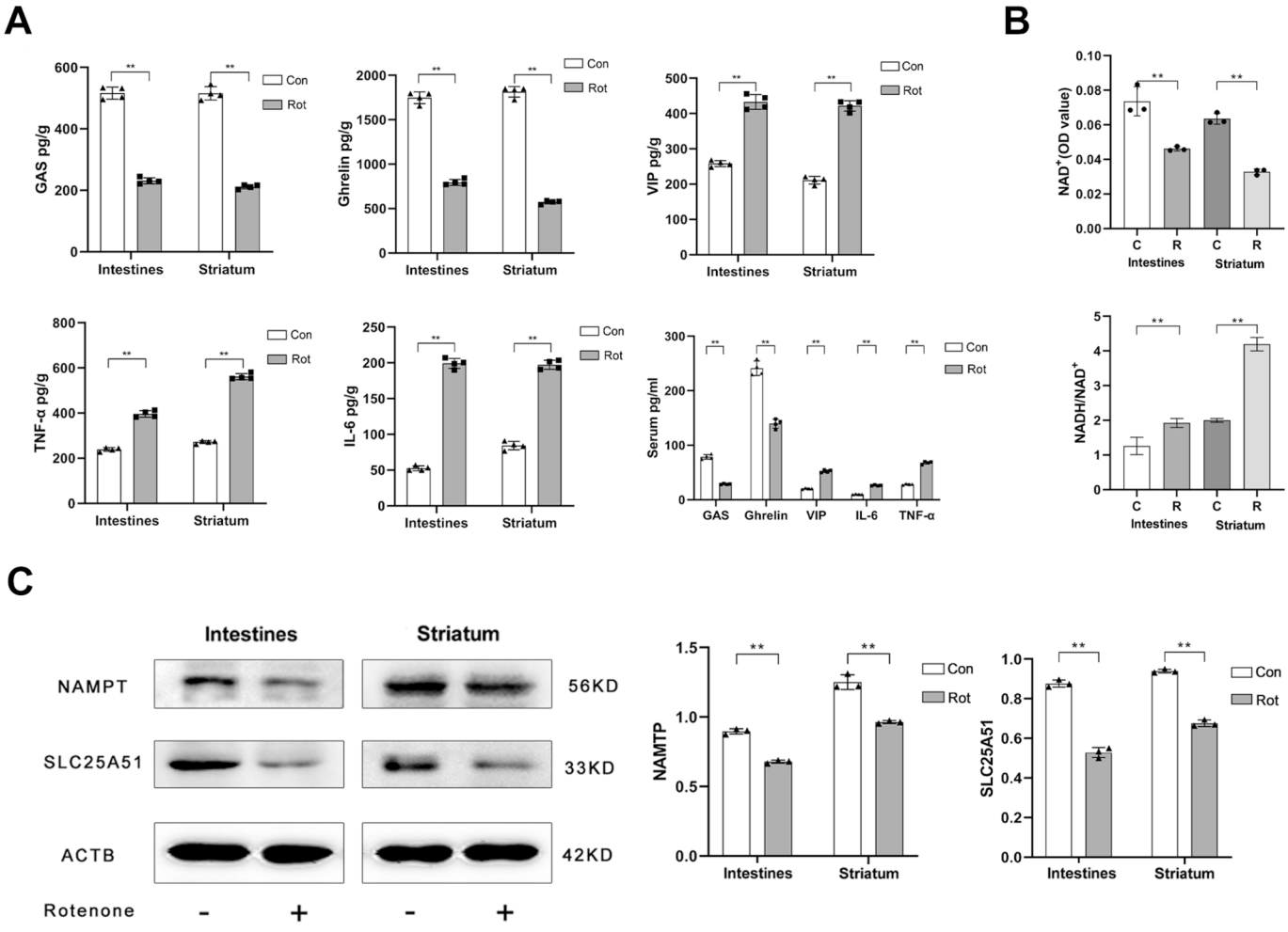

Fig. 2. The effect of rotenone exposure on the levels of brain-gut peptides and inflammatory factors in the intestinal tissues, striatal tissues and serum of rats, and its effect on NAD^+ content and related metabolism. (A) Detecting the levels of brain-gut peptides (GAS, Ghrelin, VIP) and inflammatory factors (TNF-α, IL-6) in rat intestinal tissues, striatal tissues, and serum by using Elisa's method. Con: control group, Rot: rotenone exposure group. The values represent the means ± SEM. **: $P < 0.01$, compared with control group. (B) Effect of rotenone exposure on NAD^+ content. After exposure to rotenone in rats, the NAD^+ levels and the NAD^+ /NADH ratio in intestinal and striatal tissues. C: control group, R: rotenone exposure group. These values represent the mean ± SEM.**: $P < 0.01$, compared with the control group. (C) After exposure to rotenone in rats, the protein levels of NAMPT and SLC25A51 in intestinal and striatal tissues. These values represent the mean ± SEM.**: values $P < 0.01$, compared with the control group.

electron microscopy showed that the villi of intestinal tissues were shortened, sparse, disorderly arranged and often broken, with unclear brush like edges in rats exposed to rotenone. Additionally, the mitochondria in intestinal mucosal epithelial cells of the rats exposed to rotenone showed morphological abnormalities such as shortening, swelling, and vacuolization compared with the control group. It was suggested that exposure to rotenone could damage the intestinal mucosa and barrier function, and led to varying degrees of reduction in mitochondrial area, length, and cristae length.

Effects of rotenone on the content of brain-gut peptide and inflammatory factors in intestinal tissues, striatal tissues and serum of rats respectively

In the experimental results (Fig. 2A), there was a significant decrease in the content of gastrin (GAS) and Ghrelin in the intestinal tissues, striatal tissues, and serum of rats, respectively ($P < 0.01$). In the intestinal tissues, GAS and Ghrelin decreased by an average of approximately 55 %, 55 % respectively; in the striatal tissues, GAS and Ghrelin decreased by an average of approximately 59 % and 68 % respectively; In the serum, GAS and Ghrelin decreased by an average of approximately 64 %, 42 % respectively. However, compared with the control group, there was a significant increase in the content of vasoactive intestinal peptide (VIP) in the intestinal tissues, striatal tissues, and serum of rats, respectively ($P < 0.01$). In the intestinal tissues, VIP increased by an average of approximately 40 %; in the striatal tissues, VIP increased by an average of approximately 50 %; in the serum, VIP increased by an average of approximately 61 %. As for the results of inflammatory factors in intestinal and striatal tissues, there was a significant increase in the levels of Tumor necrosis factor alpha (TNF-α) and Interleukin-6 (IL-6) in the intestinal tissues, striatal tissues, and serum of rats ($P < 0.01$). In the intestinal tissues, TNF-α and IL-6 increased by an average of approximately 40 %, 74 % respectively; in the striatal tissues, TNF-α and IL-6 increased by an average of approximately 52 % and 57 % respectively; In the serum, TNF-α and IL-6 increased by an average of approximately 59 %, 62 % respectively.

The analysis of composition of gut microbiota in rats exposed to rotenone based on metagenomic data

First, by using operational taxonomic units (OTU) (Fig. 3A), some sequencing error sequences were removed to improve the accuracy of analysis. Then, according to the annotated results, the top 10 species with the highest abundance ranking at each taxonomic level in terms of species relative abundance (species distribution) at the phylum level and genus level (Fig. 3B and C) were displayed. These were further sort out as the difference between the two groups at the phylum level and genus level (Fig. 3D and E). According to the annotation and abundance information, the top 35 genera for clustering were selected and a heat map of species abundance clustering (Fig. 3F) was drawn to discover the species level in the sample. At the phylum level, the microbiota with the highest abundance in each group were *Firmicutes* and *Bacteroidota*. Compared with the control group, the relative abundance of *Firmicutes* increased and the relative abundance of *Bacteroidota* decreased. At the genus level, the microbiota with the highest abundance in each group were *Lactobacillus* and *Dunaliella*, the relative abundance of *Lactobacillus* decreased and the relative abundance of *Dunaliella* increased.

In alpha diversity analysis, analysis indices, such as shannon, simpson, chao1, ACE, goods-coverage, and pd-whole-tree were used to reflect sample complexity (Fig. 4A). Then beta analysis was used to show the differences between different groups (Fig. 4B). The differences in significance between groups and within groups were tested, through the significant analysis of differences in community structure between groups. Further, Multi-Response Permutation Procedure (MRPP) difference analysis was used (Fig. 4C) between groups. The results suggested that there were significant differences in microbial species after rotenone exposure compared with the control group.

To screen differential microbiota, T-test, metastat analysis and Lefse analysis were used to find species with significant differences in abundance changes between groups. Among them, T-test was used to show the significantly different species found at the order, family and genus levels respectively (Fig. 5A–C). At the order level, the relative abundances such as *Erysipelotrichales*, *Bifidobacteriales* and *Alteromonadales* increased significantly. While the relative abundance of *Christensenellales* decreased significantly. At the family level, the relative abundances such as *Erysipelotrichaceae* and *Bifidobacteriaceae*, increased significantly, and the relative abundance of *Prevotellaceae* decreased significantly. At the genus level, the relative abundances such as *Dubosiella* and *Bifidobacterium*, increased significantly, and the relative abundance of *Prevotella* decreased significantly. In MetaStat analysis, three species with significant differences were screened at the genus level (Fig. 5D). *f_Erysipelotrichaceae*, *g_Dubosiella*, *f_Tannerellaceae*, and *g_Parabacteroides* significantly increased; *f_Oscillospiraceae* and *g_UCG-005* significantly decreased. Finally, the bar chart of the LDA value distribution (Fig. 5E) and the evolutionary branch chart (Fig. 5F) were drawn by Lefse analysis. The results showed that the relative abundance of *f-Erysipelotrichaceae* increased significantly and *g-Prevotellaceae* decreased significantly.

Untargeted metabolomic analysis of the gut microbiota in the feces of rotenone-exposed rats

Metabolite analysis of feces from two groups of rats

UHPLC-QE-MS was used to test the fecal samples, and the metabolites were directly evaluated. The total ion-flow chromatogram (Fig. 6A) showed that multiple metabolites (each peak representing ≥ 1 metabolite) were detected in the feces of both the control ($n = 3$) and the infected groups ($n = 3$).

The principal component analysis (PCA) (Fig. 6B) showed that each scatter represented a sample, and the color and shape of the scatter represented different groups. The fecal samples of the control group and the infected group were all within the 95 % confidence zone (Hotelling's T-squared ellipse), and the metabolism between the two groups were significantly differentiated. In order to find the real difference between the control group and the infected group and to screen for effective differential metabolites, the results were analyzed using the statistical method of orthogonal least squares discriminant analysis (OPLS-DA). The OPLS-DA plot (Fig. 6C) showed a significant separation of metabolic differences between the two groups.

The identified metabolites were classified according to the chemical classification information to form a pie chart (Fig. 6D). Different color blocks indicated different taxonomic categories in the figure, and the percentage of metabolites indicated the proportion of metabolites of that type in the number of all metabolites. The results suggested that the content of lipids was the most, up to 26.987 %. And then, the results of screening for differential metabolites were visualized in a volcano plot (Fig. 6E) containing all the substances measured in this experiment. The abscissa represented the fold change (take the bottom log of 2), the ordinate represented the P-value (take the negative number of the bottom log of 10). The scatter size represented the VIP value of the OPLS-DA model, the VIP value is greater with the larger of the scatter.

Analysis of fecal metabolites and metabolic pathways in two groups of rats

Significant differences in 118 substances ($P < 0.05$) were observed. The top 15 differential metabolites of change up and down multiple were taken to draw the matchstick map (Fig. 7A) and radar map (Fig. 7B) to show the corresponding content change trend. Next, the most significant differences between (3beta, 22E, 24R)-5,8-Epidioxy-23-methylergosta-6,22-dien-3-ol and (3beta, 22E, 24R), Ergosta-4,6,8,22-tetraen-3-ol were shown as examples, the data distribution characteristics of the same species in the control group were shown (Fig. 7C). Meanwhile, each set of identified differential metabolites was used to draw the receiver operating characteristic curves (ROC) and to calculate

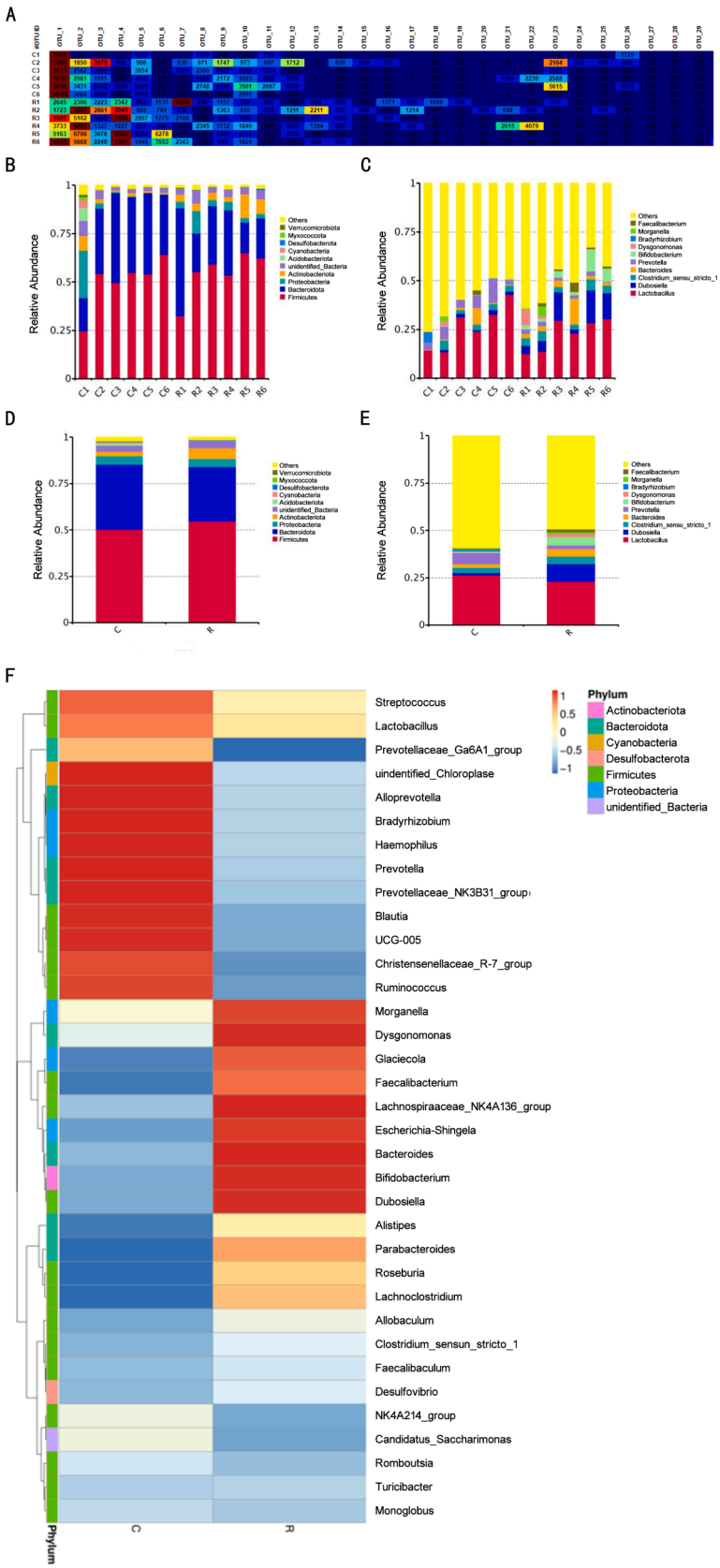

Fig. 3. Gut microbial composition of both groups of rats. (A) Annotated heatmap of operational taxonomic units. C represents the control group, R represents the rotenone exposure group, and the numbers represent different samples. (B) At the phylum level, the top 10 species with the highest abundance ranking. (C) At the genus level, the top 10 species with the highest abundance ranking. (D) At the phylum level, the relative abundance differences of species between the control group and the fish vine ketone exposure group. (E) At the genus level, the relative abundance differences of species between the control group and the rotenone exposure group. (F) Cluster heatmap of the top 35 species with the highest abundance at the genus level between the control group and the rotenone exposure group.

A

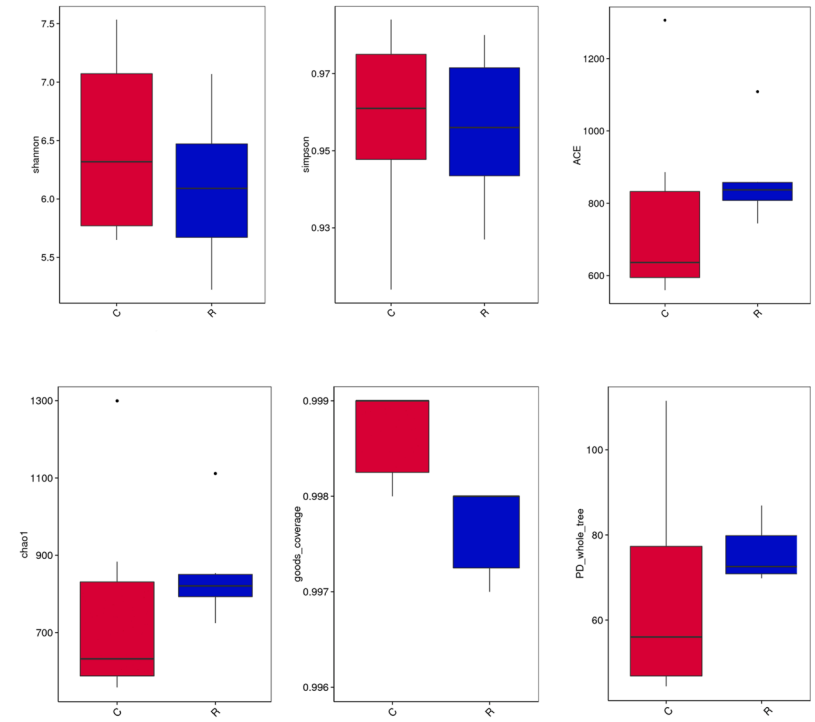

B

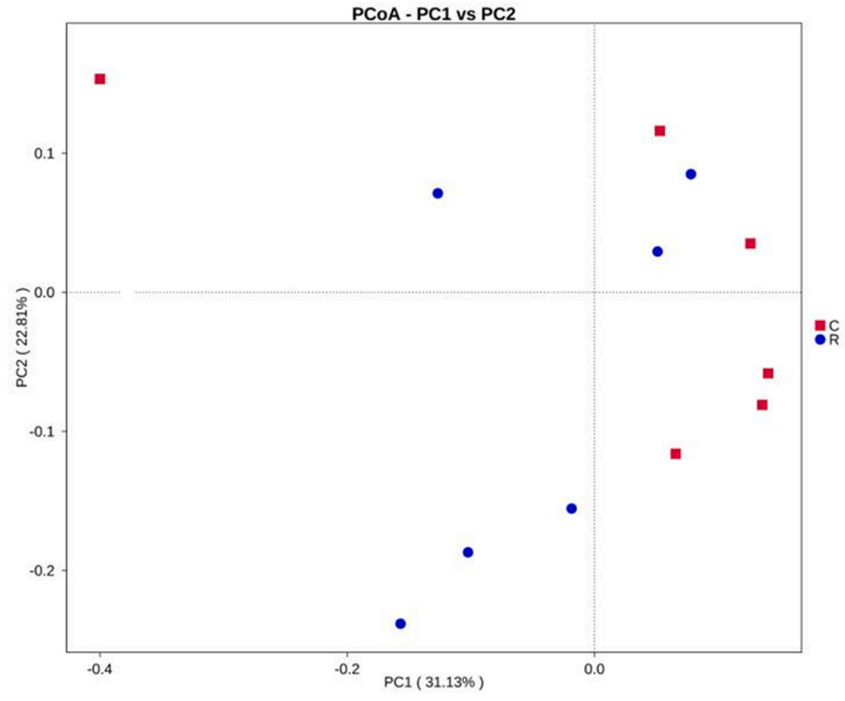

C

Multi-Response Permutation Procedure				
Group	A	observed-delta	expected-delta	Significance
Con-Rot	0.1046	0.4296	0.4798	0.003

Fig. 4. Effect of rotenone exposure on the rat gut microbiota. (A) Shannon, Simpson, Chao1, ACE, goods-coverage, and pd-whole-tree analysis indices in alpha diversity analysis. C represents the control group, R represents the rotenone exposure group. (B) Beta analysis between different groups and samples. (C) Differential analysis of MRPP between control group and rotenone exposure group.

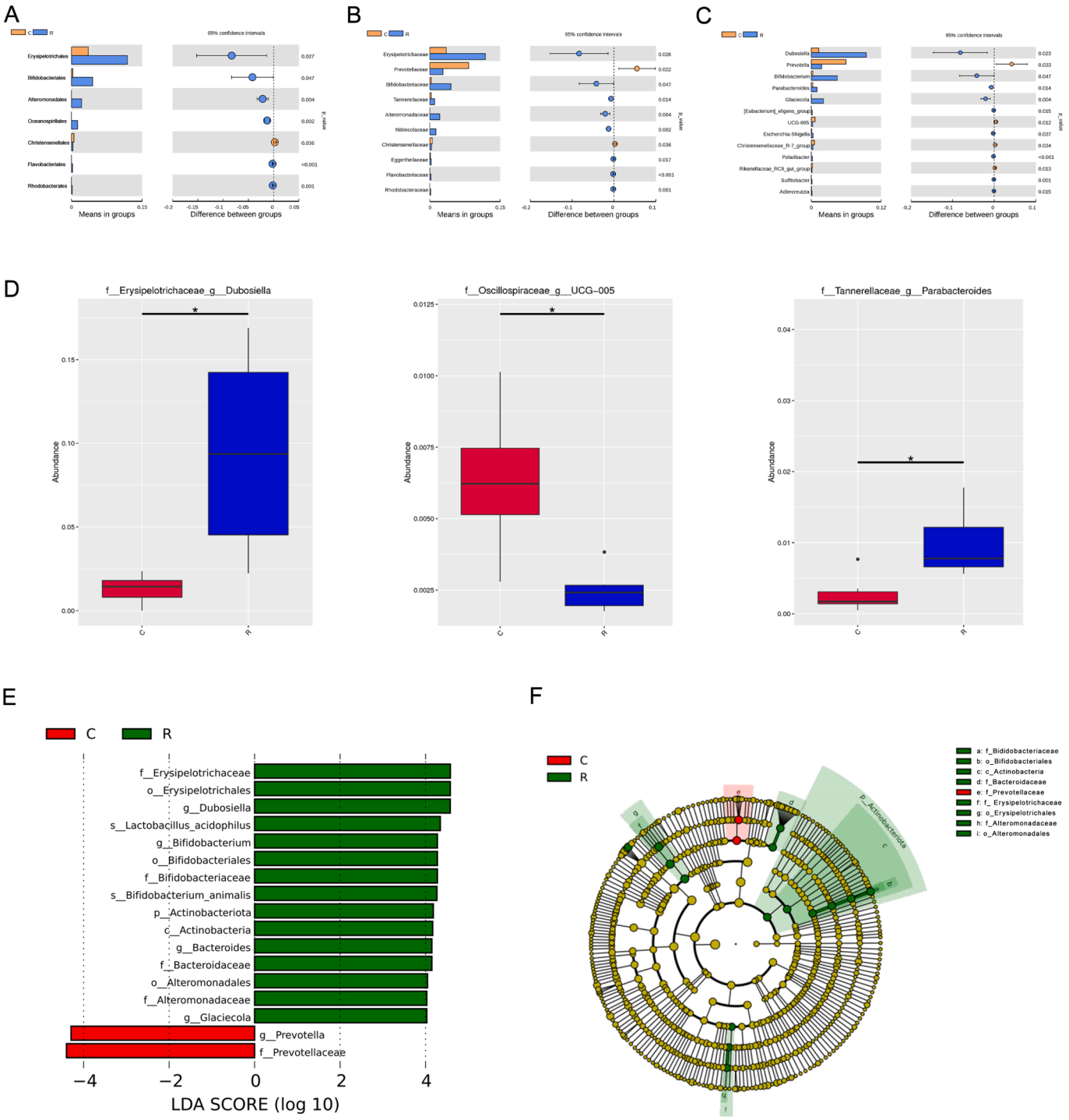

Fig. 5. Analysis of gut microbial species differences between the two groups of rats. (A) Species with significant differences identified through T-test at the order level. C represents the control group, R represents the rotenone exposure group. (B) Species with significant differences identified through T-test at the family level. (C) Species with significant differences identified through T-test at the genus level. (D) At the genus level, three significantly different species were selected through MetaStat analysis. Red indicates the control group, and blue indicates the rotenone exposure group. (E) Calculate the distribution histogram of LDA values through Lefse analysis. (F) Calculate the evolutionary branch chart of LDA values through Lefse analysis. (For interpretation of the references to color in this figure legend, the reader is referred to the web version of this article.)

the area under the curve (AUC) (Fig. 7D). In all 118 substances with significant fecal differences, the AUC was 1.

Further, the selected differential metabolites were enriched in the KEGG metabolic pathway, and the KEGG enrichment map was plotted based on the calculated Rich Factor (Fig. 7F). The results suggested that the most differences and changes were found in the steroid biosynthesis pathways. The differential abundance scores (DA Score) (Fig. 7E) was used to reflect all the differential metabolites in this pathway, which suggested that choline metabolism in cancer tended to be upregulated. And the synthesis, secretion and action of parathyroid hormone tended to be downregulated.

Finally, the differential metabolites in the authoritative metabolite databases, such as KEGG and PubChem, were maped to find the key pathways with the highest correlation with metabolite differences. The

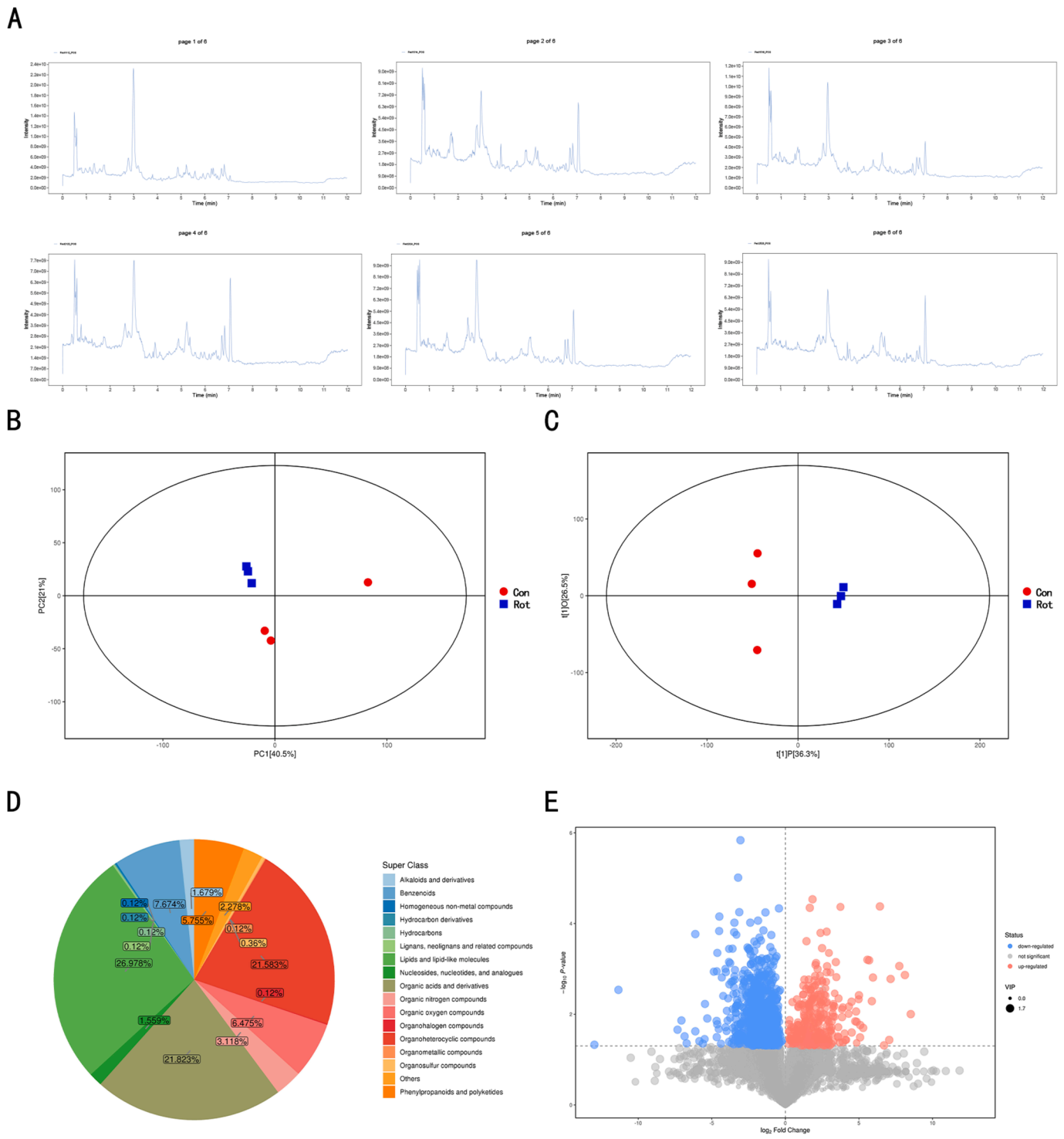

Fig. 6. Analysis of fecal metabolites in two groups of rats. (A) Comparison of fecal total ion flow chromatography between two rat groups. Control group (1–3), rotenone exposure group (4–6). (B) PCA chart of metabolite. Con indicates the control group, and Rot indicates the rotenone exposure group. (C) OPLS-DA plot of metabolite. (D) Pie plot of metabolite classification and proportion. (E) Volcano plot of the differential metabolite. Metabolites significantly up-regulated are indicated in red on the right side, down-regulated are indicated in blue on the left side and not significant are indicated in grey on the lower part. (For interpretation of the references to color in this figure legend, the reader is referred to the web version of this article.)

matching information of differential metabolites was obtained. The results of metabolic pathway analysis were plotted as pathway enrichment rectangular tree (Fig. 7G), after the search and metabolic pathway analysis in Rattus norvegicus (rat). The rectangular tree graph showed that the differential metabolites were enriched in the nicotinate and nicotinamide metabolic pathways, which had the greatest effect on the whole metabolic system. And the most significant changes were enriched in the steroid biosynthesis pathway.

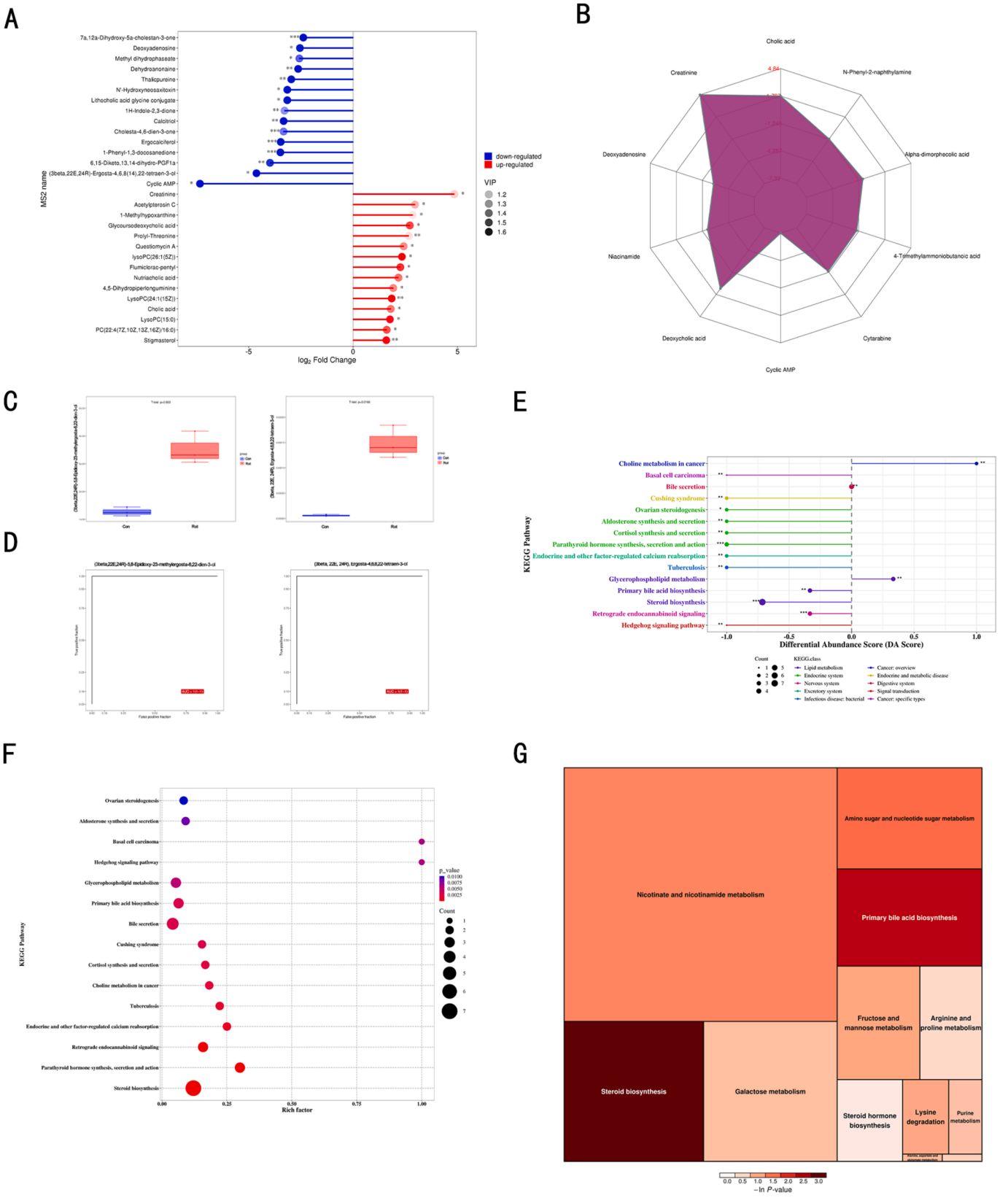

(caption on next page)

Fig. 7. Differential metabolite analysis between the control and infected groups. (A) The matchstick plot of differential metabolites between control group and rotenone exposure group. Down-regulated is blue on the left of 0, up-regulated is red on the left of 0. The abscissa shows the log-transformed multiple change. Point color shades represent the VIP value size. (B) The radar plot of differential metabolites between control group and rotenone exposure group. Each grid line represents a difference multiple, and the purple shade consists of a difference multiple line for each material. (C) The box plot of substances with the most significant differences in content. Blue indicates the control group, and red indicates the rotenone exposure group. (D) The ROC of the substance with the most significant difference in content. The ROC takes the true positive rate as the ordinate and the false positive rate as the abscissa. With an AUC greater than 0.5, the closer the AUC is to 1, the better the diagnostic effect is. When AUC equals 0.5, it indicates that the diagnostic method is completely ineffective and has no diagnostic value. (E) The differential abundance score plot. The abscissa represents the DA score, and the ordinate is the KEGG metabolic pathway ID number. A DA score equal to 1 indicates an up-regulated expression trend of all annotated differential metabolites in this pathway, and DA score Equal to −1 is the opposite. The length of the line segment represents the absolute value of DA score. The size of the dot indicates the number of differential metabolites annotated in the pathway. (F) The KEGG enrichment map. The abscissa represents the corresponding Rich Factor for each pathway, and the ordinate is the KEGG metabolic pathway ID number. The size of the dot indicates the number of differential metabolites enriched in the pathway. Colors indicate the magnitude of the p-values, the smaller the P value, the redder the color, which represents a more significant enrichment degree. (G) The rectangular treemap plot. Each block in the figure represents a metabolic pathway, the square size indicates the influence factor size of this pathway in the topological analysis, and the square colors indicate the P-values of the enrichment analysis. (For interpretation of the references to color in this figure legend, the reader is referred to the web version of this article.)

Short-chain fatty acid targeting metabolomics detection results in intestinal and striatal tissues of two groups of rats exposed to rotenone respectively

Statistics of short-chain fatty acids in intestinal and striatal tissues of both rat groups

The gas chromatography-mass spectrometry (GC–MS) was used to detect the intestinal tissues and striatal tissues samples, and the metabolites were directly evaluated. The total ion current chromatograms of intestinal tissues and striatal tissuesshowed that multiple metabolites were detected (each peak represents $\geq$ 1 metabolite)in GC–MS SIM mode (Fig. 8A and B). According to the PCA diagram and OPLS-DA diagram of intestinal tissues samples (Fig. 8C), it could be seen that the two groups of samples were very significantly distinguished, and all samples were within the 95 % confidence interval. The statistical analysis results of the detection of short-chain fatty acids could be visualized in each group in the form of a volcano plot (Fig. 8D). The results suggested that there was an increase or a decrease of the short-chain fatty acids. Metabolites with significantly up-regulation were indicated in red, and metabolites with significantly down-regulation were indicated in blue. Using the same analysis method, the PCA diagram, OPLS-DA diagram (Fig. 8E) and volcano plot (Fig. 8F) of short-chain fatty acids were obtained in striatal tissues.

Differential analysis of short chain fatty acids in intestinal and striatal tissues of rats exposed to rotenone respectively

According to the short-chain fatty acid data detected in two groups of rats, differential analysis on the same substance in the two sets of data was performed. Acetic acid and butyric acid were taken as examples and a box plot of short-chain fatty acids was made in intestinal tissues (Fig. 9A). Then the hierarchical cluster analysis was used to study the expression characteristics and the change characteristics of short-chain fatty acids between the two groups. The quantitative values of metabolites was used to calculate the Euclidean distance matrix. cluster The metabolites were clusterd by the complete linkage method, and a heat map of hierarchical cluster was drawn to analyed the short-chain fatty acids in intestinal tissues (Fig. 9B). Finally, the ROC diagram of short-chain fatty acids (Fig. 9C) was drawn in intestinal tissues and AUC was calculated to judge the diagnostic value of short-chain fatty acids in this experiment. Using the same analysis method, the box plot (Fig. 9D), heat map of hierarchical cluster analysis (Fig. 9E), and ROC diagram (Fig. 9F) of short-chain fatty acids were obtained in striatal tissues respectively. The results suggested that the contents of acetic acid and butyric acid decreased significantly ($P < 0.05$) both in intestinal tissues and striatal tissues of rats with rotenone exposure.

600MRM high-throughput targeting metabolomics detection results of intestinal and striatal tissues of rats exposed to rotenone

Raw data processing of high-throughput target quantitative metabolites in intestinal and striatal tissues of rats exposed to rotenone

Liquid chromatography-mass spectrometry (LC-MS) composite triple fourth stage rod + linear ion trap mass spectrometry (QTRAP) high-throughput target quantification method was used. Then the mass spectrometry analysis was performed using multiple reaction monitoring (MRM) mode and was directly analyzed the detection results.

By processing the raw data, a PCA graph (Fig. 10A) was drawn, which included 2 quality control (QC) samples and 12 experimental samples. A total of 363 metabolites were extracted. To better analyze the data, a series of preparation and organization (data management) were performed as the raw data. After pretreatment, 354 metabolites were retained.

The statistics of high throughput target quantitative metabolite of intestinal and striatal tissues in two groups of rats

According to the detection results of intestinal tissues samples, PCA diagrams and OPLS-DA diagrams were made (Fig. 10B). It can be seen that the two groups of samples were significantly distinguished, and all samples were within the 95 % confidence interval. The statistical analysis results were visualized in each group with a volcano plot (Fig. 10C). There were an increase or a decrease of each metabolite. Metabolites with significantly up-regulation were indicated in red, and metabolites with significantly down-regulation were indicated in blue. Finally, the PCA diagram, OPLS-DA diagram (Fig. 10D), and volcano plot (Fig. 10E) were obtained with the same analysis method.

Differential metabolites and enrichment of metabolic pathways in intestinal and striatal tissues of rats exposed to rotenone

According to the detection results of high-throughput target quantitative differential metabolites, the differential metabolites in the top 15 up-regulation and down-regulation were displayed for the results of intestinal tissues samples (Fig. 11A) and striatal tissues samples (Fig. 11E). Then hierarchical cluster analysis was carried out to draw the heat map of hierarchical cluster analysis of short-chain fatty acids in intestinal tissues (Fig. 11B) and the heat map of hierarchical cluster analysis of short-chain fatty acids in striatal tissues (Fig. 11F). The results suggested that compared with the control group, 4-methylphenol significantly increased obviously and 3-methylhistidine significantly decreased significantly in intestinal tissues. In striatal tissues, 2-thiocytidine significantly increased obviously, and isonicotinic acid significantly decreased. In addition, compared with the control group, the content of nicotinamide significantly increased ($P < 0.05$) in the intestinal tissues of rats in the rotenone exposure group. And there was also an increase in nicotinamide in striatal tissues, but there was no statistical difference. However, nicotinamide adenine dinucleotide (NAD^+) significantly decreased in striatal tissues ($P < 0.05$). And there was also a

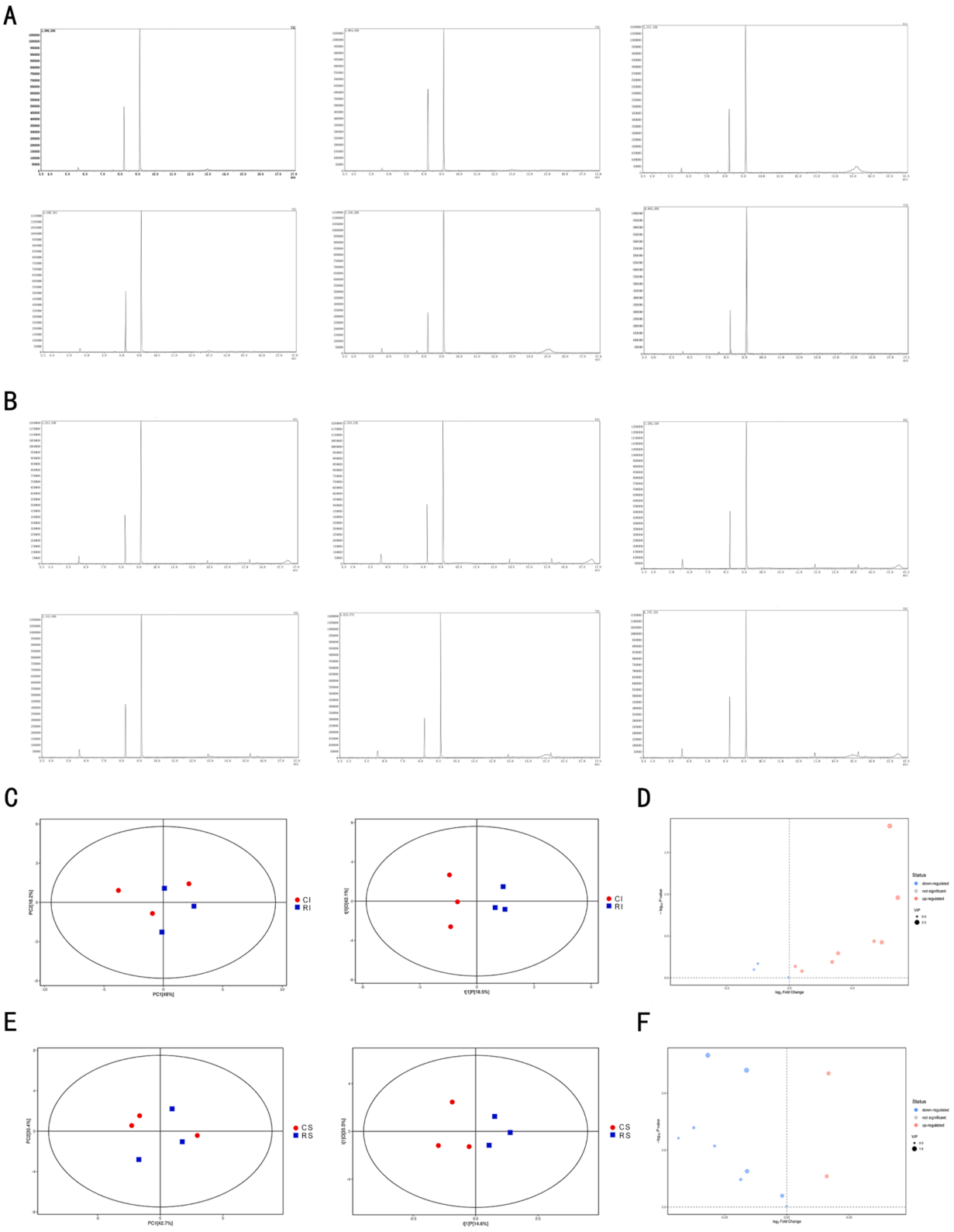

Fig. 8. Statistical data of short-chain fatty acids in the intestinal and striatal tissues of two groups of rats. (A) Total ion current chromatogram of intestinal tissues samples of two groups of rats in GC–MS SIM mode. Control group (n = 3), rotenone exposure group (n = 3). (B) Total ion current chromatogram of striatal tissues samples of two groups of rats in GC–MS SIM mode. Control group (n = 3), rotenone exposure group (n = 3). (C) PCA diagram and OPLS-DA diagram of short-chain fatty acids in intestinal tissues. CI is the control group and RI is the rotenone exposure group. (D) Volcano plot of short-chain fatty acids in intestinal tissues. Metabolites significantly up-regulated are indicated in red on the right side and down-regulated are indicated in blue on the left side. (E) PCA diagram and OPLS-DA diagram of short-chain fatty acids in striatal tissues. CS is the control group and RS is the rotenone exposure group. (F) Volcano plot of short-chain fatty acids in striatal tissues. Metabolites significantly up-regulated are indicated in red on the right side and down-regulated are indicated in blue on the left side. (For interpretation of the references to color in this figure legend, the reader is referred to the web version of this article.)

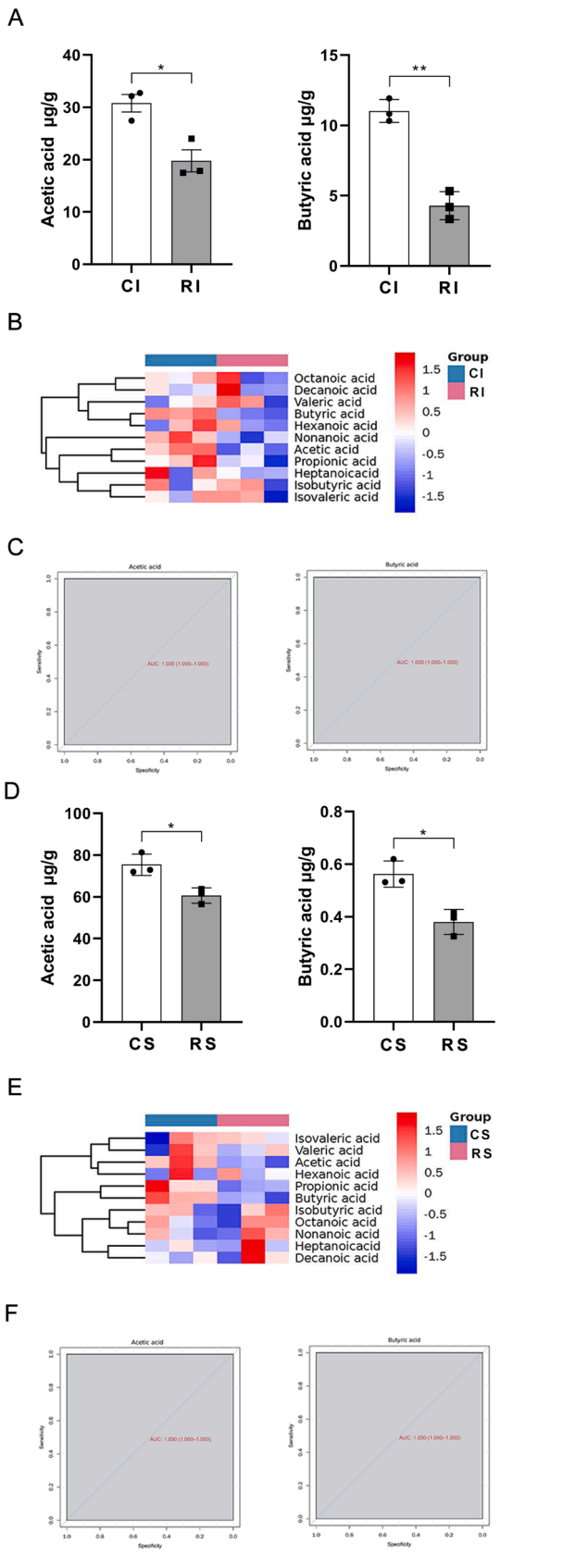

(caption on next column)

Fig. 9. Differential analysis of short-chain fatty acids in two groups. (A) Box plot of short chain fatty acids in intestinal tissues. CI is the control group and RI is the rotenone exposure group. The values represent the means ± SEM. *: $P < 0.05$, **: $P < 0.01$, compared with control group. (B) The heat map of hierarchical cluster analysis of short-chain fatty acids in intestinal tissues. CI on the left is the control group, RI on the right is the rotenone exposed group. (C) The ROC of the intestinal tissues short-chain fatty acid. Take the true positive rate as the vertical coordinate and the false positive rate as the horizontal coordinate. (D) Box plot of short chain fatty acids in striatal tissues. CS is the control group and RS is the rotenone exposure group. The values represent the means ± SEM. *: $P < 0.05$, compared with control group. (E) The heat map of hierarchical cluster analysis of short-chain fatty acids in striatal tissues. CS on the left is the control group, RS on the right is the rotenone exposed group. (F) The ROC of the striatal tissues short-chain fatty acid. Take the true positive rate as the vertical coordinate and the false positive rate as the horizontal coordinate.

decrease in intestinal tissueswithout statistical difference.

Next, according to the enrichment of differential metabolites detection in KEGG metabolic pathways, the KEGG enrichment map of differential metabolites in intestinal tissues (Fig. 11C) in striatal tissues (Fig. 11G) were drawn respectively. Finally, a further comprehensive analysis of the differential metabolic pathways was conducted to find the key pathway with the highest correlation with metabolite differences. The pathway enrichment treemap of intestinal tissues (Fig. 11D) and striatal tissues (Fig. 11H) was drawn respectively. The results suggested that the taurine and hypotaurine metabolic pathway accounted for the largest proportion among all pathways in intestinal tissues. In striatal tissues, the vitamin B6 metabolic pathway accounted for the largest proportion among all pathways. The most substances were enriched in the cysteine and methionine metabolic pathways, which was also reflected in both intestinal and striatal tissues. In addition, there was also an enrichment of differential metabolites in pathways such as pentose and glucuronic acid interconversion, arginine and proline metabolism, and nicotinic acid and nicotinamide metabolism.

Disrupted nicotinic acid and nicotinamide metabolic pathways in rats exposed to rotenone

According to the results of multi-omics, including the non-targeted metabolomics and the high-throughput targeted metabolomics, the nicotinate and nicotinamide metabolism pathways were both highly enriched, with significant changes in related differential metabolites. As shown by the treemap, the nicotinate and nicotinamide metabolism pathways had a significant impact on the metabolic changes between the control group and the rotenone-intoxicated group. Therefore, the nicotinate and nicotinamide metabolism pathways were chosen to continue experimental verification.

The level of NAD^+ and NADH were detected respectively in intestinal and striatal tissues. Results showed that there was a decrease of NAD^+ content ($P < 0.01$) and an increase of NADH/NAD^+ redox index values ($P < 0.01$) in the rotenone-intoxicated group compared with the control group (Fig. 2B). To further explore the mechanism of the decrease of NAD^+ in rotenone induced in the dopamine neuron. The expression of NAMPT and SLC25A51 was investigated in the control group and the rotenone-intoxicated group. The results suggested thatthe expression of NAMPT and SLC25A51 proteins decreased significantly in intestinal and striatal tissues of rats after rotenone exposure ($P < 0.01$) (Fig. 2C). In the intestinal tissues, NAMPT and SLC25A51 decreased by an average of approximately 24 % and 40 % respectively; in the striatal tissues, NAMPT and SLC25A51 decreased by an average of approximately 23 % and 28 % respectively. These data suggested that exposure to rotenone impacted NAD^+ biosynthesis and mitochondrial NAD^+-related metabolic pathways in the intestine and dopaminergic neurons. It reduced NAD^+ levels and raised the NADH/NAD^+ redox index.

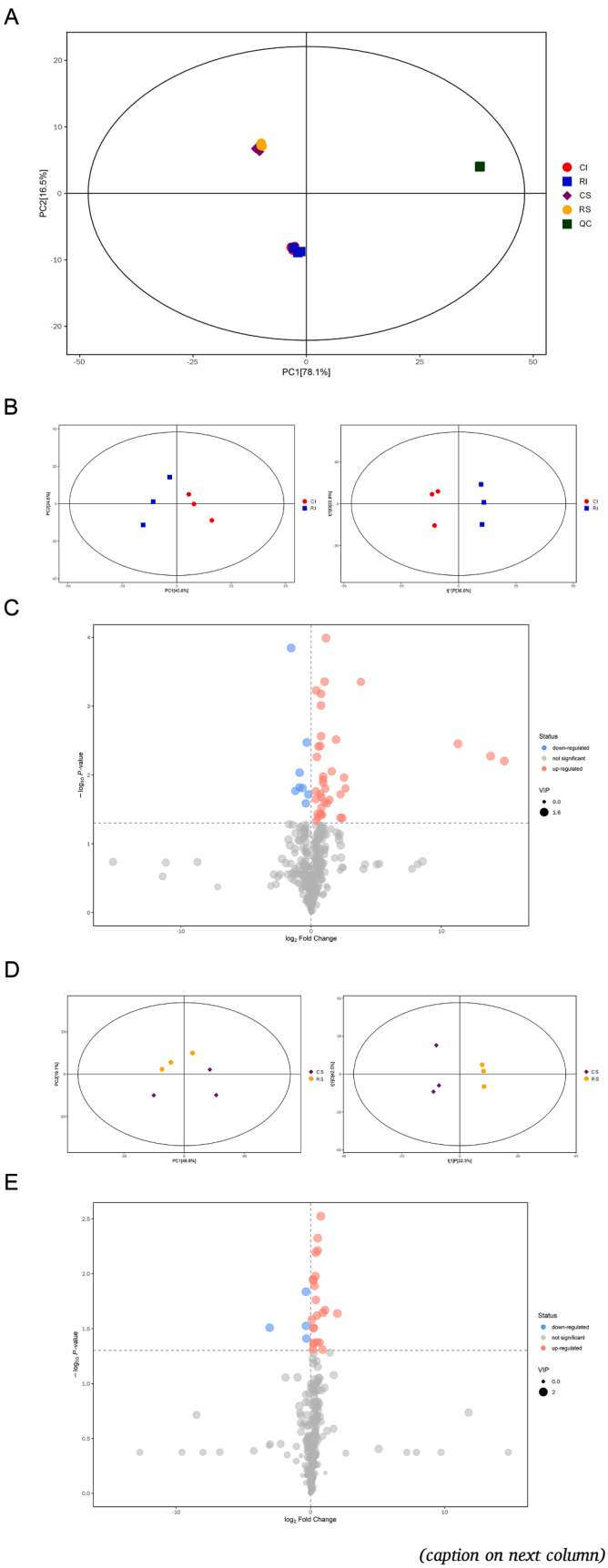

(caption on next column)

Fig. 10. Statistics of high-throughput target quantitative metabolites in intestinal tissues and striatal tissues of two groups of rats. (A) The PCA plot of the total samples. CI is the intestinal tissues of rats in the control group, RI is the intestinal tissues of rats in the rotenone exposure group, CS is the striatal tissues of rats in the control group, RS is the striatal tissues of rats in the rotenone exposure group, and green is the quality control sample. (B) PCA diagram and OPLS-DA diagram of high-throughput target quantitative metabolites in intestinal tissues. CI is the control group and RI is the rotenone exposure group. (C) Volcano plot of high-throughput target quantitative metabolites in intestinal tissues. Metabolites significantly up-regulated are indicated in red on the right side, down-regulated are indicated in blue on the left side and not significant are indicated in grey on the lower part. (D) PCA diagram and OPLS-DA diagram of high-throughput target quantitative metabolites in striatal tissues. CS is the control group and RS is the rotenone exposure group. (E) Volcano plot of high-throughput target quantitative metabolites in striatal tissues. Metabolites significantly up-regulated are indicated in red on the right side, down-regulated are indicated in blue on the left side and not significant are indicated in grey on the lower part. (For interpretation of the references to color in this figure legend, the reader is referred to the web version of this article.)

Discussion

Rotenone is a widely utilized pesticide (Greenamyre et al., 2000). However, in recent years, it has been reported that rotenone exposure is associated with neurotoxicity (Peng et al., 2016). As the inhibitor of the mitochondrial complex I, rotenone is thought to be associated with PD, particularly in sporadic PD (Tanner et al., 2011). Till now, the pathogenesis of PD is not completely understood, environmental and genetic factors are considered to play important roles in the onset of PD (Betarbet et al., 2000). Therefore, the present study explored the metabolic abnormalities in rats exposed to rotenone.

In recent years, numerous studies have indicated that the gut microbiota contains 150 times as many genes as humans. The gut microbiota plays a vital role in the human body (Milani et al., 2017). Particularly in recent years, the significant role of the gut microbiota in regulating central nervous system diseases via the "gut microbiota-intestine-brain" axis has been gradually uncovered (Góralczyk-Bińkowska et al., 2022; Quigley, 2017; Rutsch et al., 2020). Under normal circumstances, there is a dynamic equilibrium between the gut microbiota and the host. By digesting food, it provides nutrition for the human body and also plays a crucial part in maintaining the body's natural barrier, regulating the body's metabolic balance, promoting the maturation of the human immune system, and maintaining the balance of neuroendocrine system (Adak and Khan, 2019; De Filippis et al., 2019; Paone and Cani, 2020).

The animal model was established based on our previous research method. On the one hand, rats exposed to rotenone gradually showed neurological symptoms such as reduced spontaneous activity, decreased exploratory desire and behavior, and decreased standing and balance functions. On the other hand, rats exposed to rotenone gradually showed significant gastrointestinal symptoms such as reduced food and water intake, loose stools and mucus stools, and unformed feces. And the above intestinal symptoms gradually worsen with the time of rotenone exposure. Our further research showed that although there was no obvious difference in the gut microbial α diversity analysis, significant changes in gut microbiota species were observed in rats exposed to rotenone compared with the control group, showing a decrease in the relative abundances of *lactic acid bacteria*, *Bacteroidetes*, and *Prevotellaceaeand*. And an increase in the relative abundance of *Firmicutes*. *Bacteroidetes* is an important basic gut microbiota of the intestine and plays an important role in maintaining the stability and integrity of the intestinal barrier of the organism (Parker et al., 2020). *Prevotellaceae* participates in the synthesis of intestinal mucin (Zhang et al., 2023). The decrease in its abundance leads to a damage to the intestinal barrier and an increase of the permeability of intestinal mucosa, which further induces intestinal bacterial endotoxins exposure and intestinal inflammatory response and leads to overexpression of α-syn protein in the

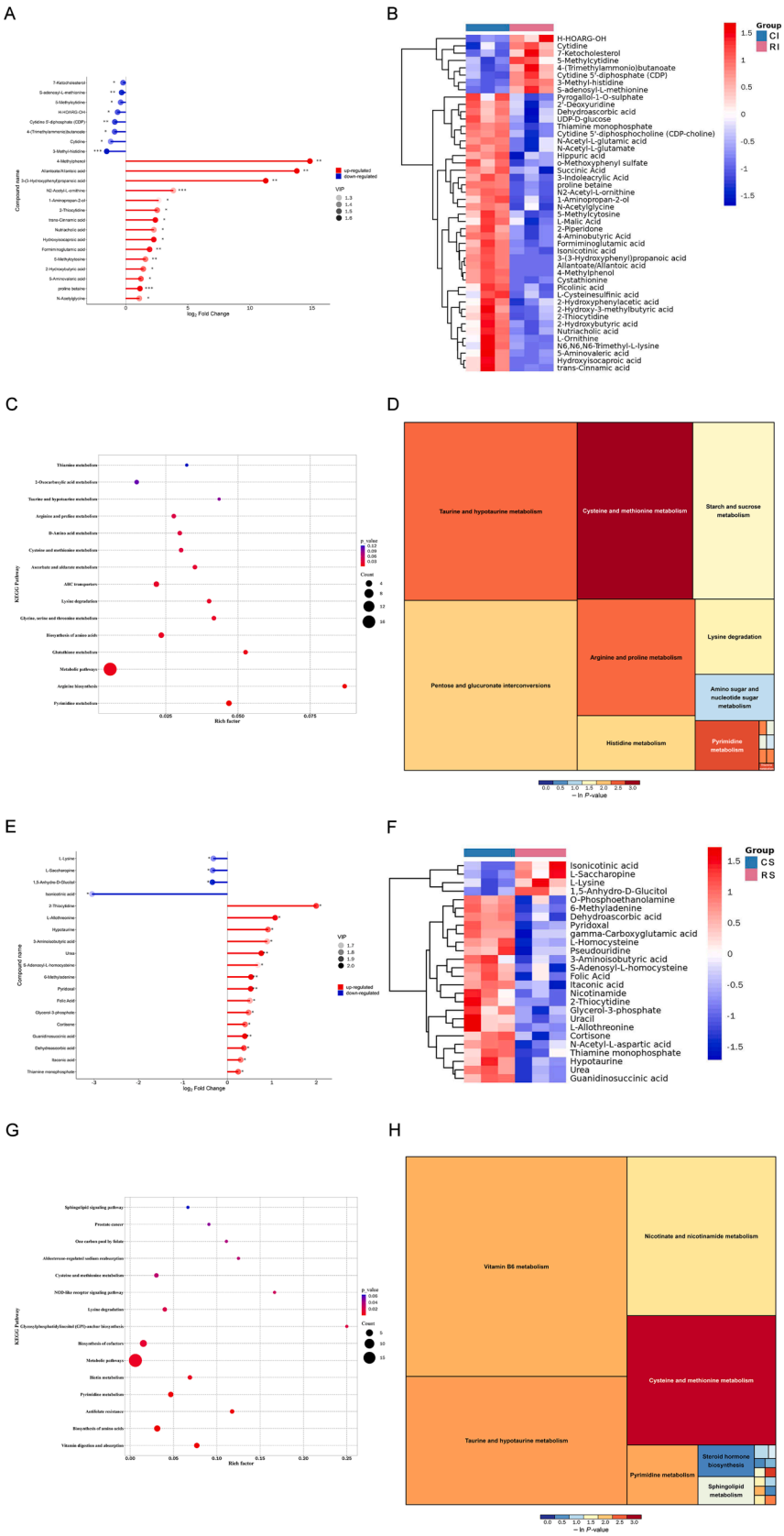

(caption on next page)

Fig. 11. Analysis of high-throughput target quantitative differential metabolites in intestinal and striatal tissues. (A) Matchstick analysis of differential metabolites in intestinal tissues. The horizontal axis displays the multiple changes after logarithmic conversion, and the depth of the dot color represents the size of the VIP value, up-regulated are indicated in red on the right side and down-regulated are indicated in blue on the left side. * represents significance. (Note: *: $P < 0.05$, **: $P < 0.01$, ***: $P < 0.001$). (B) Hierarchical Cluster Analysis of Differential Metabolites in intestinal tissues. The horizontal axis in the figure represents different experimental groups, the vertical axis represents the different metabolites compared in the group, the color blocks at different positions represent the content of corresponding metabolites. CI on the left is the intestinal tissues of rats in the control group, RI on the right is the intestinal tissues of rats in the rotenone exposure group. The red color indicates that the substance is expressed at a high level in the group, and the blue color indicates that the substance is expressed at a low level in the group. (C) KEGG enrichment analysis of differential metabolites in intestinal tissues. The horizontal axis represents the Rich Factor corresponding to each pathway, the vertical axis represents the name of the KEGG metabolic pathway, and the P-value is the P-value of Fisher's test. The size of the dot indicates the number of differential metabolites enriched in the pathway. The color represents the size of the P-value, and the smaller the P-value, the redder the color, indicating a more significant degree of enrichment. (D) Metabolic pathway analysis of differential metabolites in intestinal tissues. Each block in the rectangular tree represents a metabolic pathway, and the size of the block represents the size of the influencing factors of the pathway in topology analysis. The larger the size, the greater the influencing factors; the color of the block represents the P-value of enrichment analysis (taking negative natural logarithms, i.e. $-\ln(p)$). The darker the color, the smaller the P-value, and the more significant the enrichment degree. (E) Matchstick analysis of differential metabolites in striatal tissues. (F) Hierarchical Clustering Analysis of differential metabolites in striatal tissues. CS on the left is the striatal tissues of rats in the control group, RS on the right is the striatal tissues of rats in the rotenone exposure group. (G) KEGG enrichment analysis of differential metabolites in striatal tissues. (H) Metabolic pathway analysis of differential metabolites in striatal tissues. (For interpretation of the references to color in this figure legend, the reader is referred to the web version of this article.)

intestine and participating in the occurrence of PD regulated by brain-gut axis (Zhao et al., 2021).

However, till now, research on *Prevotella* is still very limited and it is worthy of further improvement in the future experiment. *Lactic acid bacteria*, *Bacteroidetes*, *Prevotellaceae* and other bacterial communities can produce short chain fatty acids during their carbohydrate metabolism. Therefore, the decrease in their abundance in the intestine leads to a reduction in the synthesis of short chain fatty acids, resulting in a weakened immune regulation and anti-inflammatory effect of short chain fatty acids on the intestinal and nervous system (Solch et al., 2022; Yemula et al., 2021). Consistently, butyric acid and acetic acid, as important components of short chain fatty acids, significantly decreased in rats exposed to rotenone compared with the control group. Further research showed a significant increase in inflammatory factors, such as IL-6 and TNF-α in intestinal tissues, serum, and striatal tissues in rats exposed to rotenone respectively.

Some studies believe that the ratio of *Firmicutes* to *Bacteroidetes* can be used as an important indicator to evaluate the balance of gut microbiota (Magne et al., 2020). The relative increase of *Firmicutes* will enhance the fermentation of carbohydrates and accelerate the digestion and absorption of carbohydrates in the intestine, which may lead to a faster and greater increase in blood sugar levels and bring greater pressure to the body's blood sugar regulation mechanism. This conclusion also has been confirmed by the relatively increased *Firmicutes* in metabolic diseases such as obesity and diabetes (James et al., 2022; Jordan et al., 2023). In this untargeted metabolomics of gut microbiota and high-throughput targeted metabolomics of intestinal tissues, a significant increase in UDP-D-glucose also occurred. At the same time, in the previous studies by others, it was also found that the genera *Blautia*, *Coprococcus, Roseburia*, and *Prevotella* were significantly reduced, while the abundances of *Ralstonia* and *Enterobacter* increased in the intestines of PD patients. These changes directly affect the content of their metabolites and cause changes in brain-gut peptides or inflammation in gut microbiota (Boertiena et al., 2019; Sampson et al., 2016; Vascellari et al., 2020). These experimental results further prove the important role of gut microbiota in the pathogenesis of PD.

In recent years, the interaction between SCFAs and gut microbiota has become the focus of scholars. SCFAs are formed by the fermentation of dietary fiber and resistant starch by microorganisms in the intestine (Deehan et al., 2020; Fusco et al., 2023). On the one hand, SCFAs are important for balancing metabolism and energy (Ikeda et al., 2022). On the other hand, SCFAs are also important elements for maintaining the dynamic balance of gut microbiota and regulating the intestinal mucosal barrier, and they are also an important energy source for gut microbiota and intestinal epithelial cells (Takiishi et al., 2017). In the targeted metabolic detection of short-chain fatty acids in intestinal tissues, a significant decrease in the content of butyric acid was further detected. In addition, the content of acetic acid also showed a significant downward trend.

Further non-targeted metabolite detection of rat feces was carried out. The experimental results showed that a total of 118 metabolites were observed with significant differences in rats with rotenone exposure in contrast with the control group. Among them, the content of lipids and lipid-like substances was the highest. The content of butyric acid decreased significantly. Previous studies have suggested that acetic acid was the most abundant short-chain fatty acid in human intestines and plasma, which also could play a neuroprotective role in the central nervous system through penetrating the blood–brain barrier (He et al., 2024). In previous studies, it was also found that the level of acetic acid was reduced, while the level of plasma acetic acid was significantly increased in the feces of PD patients. It is speculated that this may be related to the destruction of the intestinal barrier in PD patients, leading to more acetic acid in the intestine entering the bloodstream (Cansiz et al., 2023; Chen et al., 2022). At the same time, studies have confirmed that butyric acid could play a neuroprotective role in PD through improving intestinal barrier function, reducing inflammatory reactions, and antioxidative stress (Canani et al., 2011; Stoeva et al., 2021). At present, the content of butyric acid was reduced in the intestinal tissues of the rats exposed to rotenone in our research, which might further lead to weakened intestinal tissues barrier function and aggravate inflammatory reactions in rats exposed to rotenone compared with the control group (Su et al., 2021). In previous studies, the same changes in intestinal tissues of Parkinson's patients have also been reported (Clairembault et al., 2015). Tight junction proteins (ZO-1, Occuldin, Claudin-1) decreased, intestinal villi shorten, and the intestinal tissues structure was damaged in the intestinal tissues of rats in the rotenone exposure group in contrast with the control group. The contents of IL-6 and TNF-α were also increased in the intestines, striatum, and blood of rats exposed to rotenone respectively.

It is worth noting that butyric acid is mainly generated by Firmicutes through the butyric acid kinase pathway and the butyryl-CoA and acetyl-CoA transferase pathways (Anand et al., 2016). However, the relative abundance of Firmicutes increased in the intestines of rats after rotenone exposure. Based on the existing experimental data, it is speculated that it may be due to the comprehensive factors such as gut microbiota imbalance or dysfunction of *Firmicutes* metabolism, leading to a decrease in the content of intestinal short-chain fatty acid butyric acid. In addition, some studies have shown that intestinal bacteria could produce SCFAs and participate in the secretion of brain-gut peptides by intestinal endocrine cells (Ikeda et al. 2022). Our research also showed that rotenone poisoning could affect the content of brain-gut peptides in rat intestinal and striatal tissues respectively. These experimental results all further confirmed that the decrease in SCFA levels might lead to intestinal microbial imbalance in rotenone-poisoned rats and might damage the intestinal mucosal barrier, exacerbating the chronic inflammatory state of rat intestinal and striatal tissues.

Further analysis showed that the differential metabolites were enriched in the nicotinate and nicotinamide metabolism pathways, which had the greatest impact on the entire metabolic change system with non-targeted metabolite detection of rat feces. Moreover, the same conclusion could be gained in the experiment of high-throughput targeted metabolomics detection of striatal tissues in rats exposed to rotenone compared with the rats of the control group. It is known that nicotinamide adenine dinucleotide (NAD^+) and nicotinamide adenine dinucleotide phosphate ($NADP^+$) are produced through the nicotinate and nicotinamide metabolic pathways (Murthy et al., 2021; Ryrie and Scott, 1969). NAD^+ and $NADP^+$ both play key roles in cell energy metabolism, redox reactions, and DNA repair and so on (Canto et al., 2015; VanLinden et al., 2015). The changes in the nicotinate and nicotinamide metabolism pathway could directly affect the synthesis of NAD^+ and $NADP^+$, further disrupting the energy supply and the normal physiological functions of cells. It could be confirmed that abnormal cell energy metabolism, neuronal degeneration and death were observed in PD patients (Weintraub et al., 2022). Additionally, the metabolites of gut microbiota can affect brain function through the gut-brain axis (Góralczyk-Bińkowska et al., 2022). In our experiments, the changes enriched in the nicotinate and nicotinamide metabolism pathway were found in the non-targeted metabolomics detection of rat gut microbiota, which also suggested that gut microbiota might participate in the pathogenesis of PD by affecting this metabolism pathway. In addition, the striatum, as an important part of the basal ganglia, receives excitatory inputs from the cerebral cortex and projections from dopaminergic neurons in the substantia nigra pars compacta. It plays a key role in motor regulation (Di Tella et al., 2021). Abnormal function of the striatum will directly lead to the typical motor symptoms of PD (Mura et al., 1998; Sanchez-Catasus et al., 2022). Changes enriched in the nicotinate and nicotinamide metabolism pathway were also found in the high-throughput targeted metabolomics detection of the striatum, indicating that this pathway might also play a certain role in the motor dysfunction of PD. The reason may be that the abnormality of this metabolic pathway leads to the metabolic imbalance of neurotransmitters in the striatum, affecting the signal transmission between neurons and thus causing neuronal dysfunction. Those results suggested that there were multiple connections between the nicotinate and nicotinamide metabolism pathway and PD. In-depth study of this metabolic pathway is expected to provide new ideas and methods for the diagnosis and treatment of PD.

In the high-throughput targeted metabolomics detection of striatum, nicotinamide (NAM), a key precursor substance of NAD^+, showed a significant increase. And NAM synthesizes NAD^+ through NAMPT, the key rate-limiting enzyme for NAD^+ anabolic metabolism (Garten et al., 2015; Wang et al., 2022). It was further detected a decrease in the levels of NAD^+ in the intestinal and striatal tissues of rotenone-poisoned rats. Moreover, the NADH/NAD^+ ratio also showed a significant increase in the intestinal and striatal tissues of rotenone-poisoned rats. The NADH/NAD^+ ratio can reflect the redox state of cells, which also suggests that rotenone poisoning can lead to the state of oxidative stress in rats (Lu et al., 2014). Monitoring the NADH/NAD^+ ratio can also be one of the indicators for evaluating the condition and treatment effect of PD. Further research showed that the expression level of NAMPT, the rate-limiting enzyme for NAD^+ anabolic metabolism, was reduced, and the expression level of SLC25A51, the solute carrier protein for NAD^+ entering mitochondria, was also decreased significantly in rats exposed to rotenone. Therefore, it could be inferred that the expression of key molecules for NAD^+ synthesis decreases, which might lead to an increase in the content of synthetic substrate NAM and a decrease in NAD^+ content. At the same time, the decrease in the expression level of SLC25A51 may lead to a decrease in NAD^+ content in mitochondria, further disrupting mitochondrial energy metabolism (Girardi et al., 2020; Ziegler et al., 2021).

The above results all suggested that there were many substances in the nicotinate and nicotinamide metabolism pathway, which were importantly related to neurodegenerative diseases and have non-negligible research value. Combining the connection between this pathway and the rotenone-induced PD like disease, further analysis was carried out on the significantly different metabolites screened out through this experiment. Many previous studies have proved that oxidative stress played an important role in neurodegenerative diseases. The protein damage caused by it increases the accumulation of age-dependent protein aggregates with functional disorders, such as Tau, Aβ and so on (Koopman et al., 2022; Singh et al., 2019; Thompson et al., 2020). At the same time, excessive reactive oxygen species (ROS) will further damage neurons, which was also an important characteristic of neurodegenerative diseases (Yeung et al., 2021; Zhou et al., 2022). As a coenzyme that provides catalytic substrates in cellular redox reactions or a carrier signal molecule in cellular electron transfer reactions, NAD^+ is a key electron pair for maintaining the balance between the oxidation system and the antioxidant system (Hassinen, 2019). It can maintain redox balance and participate in the antioxidant system by regulating the activities of antioxidant enzymes such as superoxide dismutase (SOD) and glutathione peroxidase (GPx) (Roberts et al., 2006). At the same time, NAD^+ is also involved in the DNA repair process and maintains genomic stability. Previous studies have suggested that the occurrence of PD is related to gene mutations and genomic instability. NAD^+-dependent DNA repair enzymes, such as poly (ADP-ribose) polymerase (PARP), play an important role in repairing DNA damage. When the level of NAD^+ decreases, the body's DNA repair ability will be weakened, which may further increase the risk of developing PD (Ruszkiewicz et al., 2022).

This study further expands on previous research and fully reveals the relevant mechanisms of rotenone poisoning. The significantly different gut microbiota, metabolites, and metabolic pathways screened out also provided new ideas for the study of rotenone-induced neurotoxicity.

Although our study has provided valuable insights, it has certain limitations. In this study, the rotenone poisoning models in rats may not completely reproduce the complex human physiological environment. Future studies could focus on validating our findings in more advanced models or in clinical samples. Additionally, further investigations are needed to explore the potential crosstalk between the gut microbiota and other metabolic pathways that may be involved in rotenone-induced neurotoxicity.

CRediT authorship contribution statement

Yan Sai: Conceptualization, Datacuration, Investigation, Funding acquisition, Project administration, Resources, Supervision, Writing-review & editing. **Wei Ge:** Conceptualization, Datacuration, Investigation, Methodology, Software, Validation, Visualization, Writing-original draft, Writing-review & editing. **Li Zhong:** Datacuration, Formal analysis, Investigation, Methodology, Software, Validation. **Qifu Zhang:** Methodology. **Jingsong Xiao:** Methodology. **Yaohui Shan:** Methodology. **Wenqi Ye:** Methodology. **Haoyin Liu:** Methodology. **Shulin Liu:** Methodology. **Feng Ye:** Project administration, Supervision. **Xiaogang Wang:** Project administration, Supervision. **He Tang:** Project administration, Supervision. **Yuanpeng Zhao:** Project administration, Supervision. **Guorong Dan:** Project administration, Supervision.

Funding

This work was supported by The National Natural Science Foundation of China (Grant No. 81973090). Author Yan Sai has received this research support.

Declaration of competing interest

The authors declare that they have no known competing financial interests or personal relationships that could have appeared to influence the work reported in this paper.

Appendix A. Supplementary data

Supplementary data to this article can be found online at https://doi.org/10.1016/j.crtox.2024.100212.

Data availability

Data will be made available on request.

References

Adak, A., Khan, M.R., 2019. An insight into gut microbiota and its functionalities. Cell Mol. Life Sci. 76, 473–493. https://doi.org/10.1007/s00018-018-2943-4.

Anand, S., Kaur, H., Mande, S.S., 2016. Comparative in silico analysis of butyrate production pathways in gut commensals and pathogens. Front. Microbiol. 7, 1945. https://doi.org/10.3389/fmicb.2016.01945.

Betarbet, R., Sherer, T.B., Greenamyre, J.T., 2000. Animal models of Parkinson's disease. Bioessays. https://doi.org/10.1002/bies.10067.

Boertiena, J.M., Pereira, P.A.B., Aho, V.T.E., Scheperjansc, F., 2019. Increasing comparability and utility of gut microbiome studies in Parkinson's disease: a systematic review. J. Parkinson's Dis. https://doi.org/10.3233/JPD-191711.

Canani, R.B., Costanzo, M.D., Leone, L., Pedata, M., Meli, R., Calignano, A., 2011. Potential beneficial effects of butyrate in intestinal and extraintestinal diseases. World J. Gastroenterol. 17, 1519–1528. https://doi.org/10.3748/wjg.v17.i12.1519.

Cansiz, D., Unal, I., Beler, M., Ustundag, U.V., Ak, E., Emekli-Alturfan, E., Alturfan, A.A., 2023. The effect of acetic acid-induced pain in Parkinson's disease model in zebrafish. Neurotoxicology (Park Forest South) 99, 14–23. https://doi.org/10.1016/j.neuro.2023.09.004.

Canto, C., Menzies, K.J., Auwerx, J., 2015. NAD(+) metabolism and the control of energy homeostasis: a balancing act between mitochondria and the nucleus. Cell Metab. 22, 31–53. https://doi.org/10.1016/j.cmet.2015.05.023.

Chen, S.J., et al., 2022. Association of fecal and plasma levels of short-chain fatty acids with gut microbiota and clinical severity in patients with Parkinson disease. Neurology 98, e848–e858. https://doi.org/10.1212/WNL.0000000000013225.

Clairembault, T., et al., 2015. Structural alterations of the intestinal epithelial barrier in Parkinson's disease. Acta Neuropathol. Commun. 3, 12. https://doi.org/10.1186/s40478-015-0196-0.

Coulom, H., Birman, S., 2004. Chronic exposure to rotenone models sporadic Parkinson's disease in Drosophila melanogaster. J. Neurosci. 24, 10993–10998. https://doi.org/10.1523/JNEUROSCI.2993-04.2004.

De Filippis, F., et al., 2019. Distinct genetic and functional traits of human intestinal Prevotella copri strains are associated with different habitual diets. Cell Host Microbe 25, 444–453. https://doi.org/10.1016/j.chom.2019.01.004.

Deehan, E.C., et al., 2020. Precision microbiome modulation with discrete dietary fiber structures directs short-chain fatty acid production. Cell Host Microbe 27, 389–404. https://doi.org/10.1016/j.chom.2020.01.006.

Di Monte, D.A., 2003. The environment and Parkinson's disease: is the nigrostriatal system preferentially targeted by neurotoxins? Lancet Neurol 2, 531–538. https://doi.org/10.1016/s1474-4422(03)00501-5.

Di Tella, S., et al., 2021. The role of the dorsal striatum in the recognition of emotions expressed by voice in Parkinson's disease. Neurol. Sci. 42, 2085–2089. https://doi.org/10.1007/s10072-020-04959-5.

Fusco, W., et al., 2023. Short-chain fatty-acid-producing bacteria: key components of the human gut microbiota. Nutrients 15, 2211. https://doi.org/10.3390/nu15092211.

Garten, A., Schuster, S., Penke, M., Gorski, T., de Giorgis, T., Kiess, W., 2015. Physiological and pathophysiological roles of NAMPT and NAD metabolism. Nat. Rev. Endocrinol. 11, 535–546. https://doi.org/10.1038/nrendo.2015.117.

Girardi, E., et al., 2020. Epistasis-driven identification of SLC25A51 as a regulator of human mitochondrial NAD import. Nat. Commun. 11. https://doi.org/10.1038/s41467-020-19871-x.

Góralczyk-Bińkowska, A., Szmajda-Krygier, D., Kozłowska, E., 2022. The microbiota–gut–brain axis in psychiatric disorders. Int. J. Mol. Sci. 23, 11245. https://doi.org/10.3390/ijms231911245.

Greenamyre, J.T., Betarbet, R., Sherer, T.B., MacKenzie, G., Garcia-Osuna, M., Panov, A. V., 2000. Chronic systemic pesticide exposure reproduces features of Parkinson's disease. Nat. Neurosci. 3, 1301–1306. https://doi.org/10.1038/81834.

Guo, Z., Ruan, Z., Zhang, D., Liu, X., Hou, L., Wang, Q., 2022. Rotenone impairs learning and memory in mice through microglia-mediated blood brain barrier disruption and neuronal apoptosis. Chemosphere 291, 132982. https://doi.org/10.1016/j.chemosphere.2021.132982.

Hassinen, I.E., 2019. Signaling and regulation through the NAD+ and NADP+ networks antioxid redox. Sign 30, 857–874. https://doi.org/10.1089/ars.2017.7479.

He, Q., et al., 2024. Acetate enables metabolic fitness and cognitive performance during sleep disruption. Cell Metab. 36, 1998–2014. https://doi.org/10.1016/j.cmet.2024.07.019.

Ibarra-Gutiérrez, M.T., Serrano-García, N., Orozco-Ibarra, M., 2023. Rotenone-induced model of Parkinson's disease: beyond mitochondrial complex I inhibition. Mol. Neurobiol. 60, 1929–1948. https://doi.org/10.1007/s12035-022-03193-8.

Ikeda, T., Nishida, A., Yamano, M., Kimura, I., 2022. Short-chain fatty acid receptors and gut microbiota as therapeutic targets in metabolic, immune, and neurological diseases. Pharmacol. Ther. 239, 108273. https://doi.org/10.1016/j.pharmthera.2022.108273.

James, M.M., et al., 2022. Role of butyrogenic Firmicutes in type-2 diabetes. J. Diabetes Metab. Disord. 21, 1873–1882. https://doi.org/10.1007/s40200-022-01081-5.

Jordan, C.K.I., Brown, R.L., Larkinson, M.L.Y., Sequeira, R.P., Edwards, A.M., Clarke, T. B., 2023. Symbiotic Firmicutes establish mutualism with the host via innate tolerance and resistance to control systemic immunity. Cell Host Microbe 31, 1433–1449. https://doi.org/10.1016/j.chom.2023.07.008.

Koopman, M.B., Ferrari, L., Rüdiger, S.G.D., 2022. How do protein aggregates escape quality control in neurodegeneration? Trends Neurosci. 45, 257–271. https://doi.org/10.1016/j.tins.2022.01.006.

Kraeuter, A., Guest, P.C., Sarnyai, A.Z.N., 2019. The open field test for measuring locomotor activity and anxiety-like behavior. In: Guest, P.C. (Ed.), Pre-Clinical Models Techniques and Protocols, pp. 99–104.

Lu, M., Zhu, X.H., Zhang, Y., Chen, W., 2014. Intracellular redox state revealed by in vivo31P MRS measurement of NAD+ and NADH contents in brains. Magn. Reson. Med. 71, 1959–1972. https://doi.org/10.1002/mrm.24859.

Magne, F., Gotteland, M., Gauthier, L., Zazueta, A., Pesoa, S., Navarrete, P., Balamurugan, R., 2020. The firmicutes/bacteroidetes ratio: a relevant marker of gut dysbiosis in obese patients? Nutrients 12, 1474. https://doi.org/10.3390/nu12051474.

Milani, C., et al., 2017. The first microbial colonizers of the human gut: composition, activities, and health implications of the infant gut microbiota. Microbiol. Mol. Biol. Res. 81. https://doi.org/10.1128/MMBR.00036-17.

Morris, H.R., Spillantini, M.G., Sue, C.M., Williams-Gray, C.H., 2024. The pathogenesis of Parkinson's disease. Lancet 403, 293–304. https://doi.org/10.1016/S0140-6736(23)01478-2.

Mura, A., Feldon, J., Mintz, M., 1998. Reevaluation of the striatal role in the expression of turning behavior in the rat model of Parkinson's disease. Brain Res. 808, 48–55. https://doi.org/10.1016/S0006-8993(98)00791-4.

Murthy, S., Thakur, S., Kumar, A., Gupta, S., 2021. Nicotinic acid, its mechanism of action and pharmacological effects. Int. J. Multidiscip. https://doi.org/10.31305/rrijm.2021.v06.i05.007.

Paone, P., Cani, P.D., 2020. Mucus barrier, mucins and gut microbiota: the expected slimy partners? Gut 69, 2232–2243. https://doi.org/10.1136/gutjnl-2020-322260.

Parker, B.J., Wearsch, P.A., Veloo, A.C.M., Rodriguez-Palacios, A., 2020. The genus alistipes: gut bacteria with emerging implications to inflammation, cancer, and mental health. Front Immunol 11, 906. https://doi.org/10.3389/fimmu.2020.00906.

Peng, K., et al., 2016. Resveratrol regulates mitochondrial biogenesis and fission/fusion to attenuate rotenone-induced neurotoxicity. Oxid. Med. Cell Longev. 2016, 1–12. https://doi.org/10.1155/2016/6705621.

Peng, K., et al., 2018. Mitochondrial ATP-sensitive potassium channel regulates mitochondrial dynamics to participate in neurodegeneration of Parkinson's disease. Biochim. Biophys. Acta (BBA) 1864, 1086–1103. https://doi.org/10.1016/j.bbadis.2018.01.013.

Prut, L., Belzung, C., 2003. The open field as a paradigm to measure the effects of drugs on anxiety-like behaviors: a review. Eur. J. Pharmacol. 463, 3–33. https://doi.org/10.1016/S0014-2999(03)01272-X.

Quigley, E.M.M., 2017. Microbiota-brain-gut axis and neurodegenerative diseases. Curr. Neurol. Neurosci. 17. https://doi.org/10.1007/s11910-017-0802-6.

Roberts, C.K., Barnard, R.J., Sindhu, R.K., Jurczak, M., Ehdaie, A., Vaziri, N.D., 2006. Oxidative stress and dysregulation of NAD(P)H oxidase and antioxidant enzymes in diet-induced metabolic syndrome. Metab. Clin. Exp. 55, 928–934. https://doi.org/10.1016/j.metabol.2006.02.022.

Ruszkiewicz, J.A., Burkle, A., Mangerich, A., 2022. Fueling genome maintenance: on the versatile roles of NAD(+) in preserving DNA integrity. J. Biol. Chem. 298, 102037. https://doi.org/10.1016/j.jbc.2022.102037.

Rutsch, A., Kantsjö, J.B., Ronchi, F., 2020. The gut-brain axis: how microbiota and host inflammasome influence brain physiology and pathology. Front. Immunol. 11, 604179. https://doi.org/10.3389/fimmu.2020.604179.

Ryrie, I.J., Scott, K.J., 1969. Nicotinate, quinolinate and nicotinamide as precursors in the biosynthesis of nicotinamide-adenine dinucleotide in barley. Biochem. J. 115, 679–685. https://doi.org/10.1042/bj1150679.

Sampson, T.R., et al., 2016. Gut microbiota regulate motor deficits and neuroinflammation in a model of Parkinson's disease. Cell 167, 1469–1480. https://doi.org/10.1016/j.cell.2016.11.018.

Sanchez-Catasus, C.A., Bohnen, N.I., D'Cruz, N., Müller, M.L.T.M., 2022. Striatal acetylcholine-dopamine imbalance in parkinson disease: in vivo neuroimaging study with dual-tracer PET and dopaminergic PET-informed correlational tractography. J. Nucl. Med. 63, 438–445. https://doi.org/10.2967/JNUMED.121.261939.

Singh, A., Kukreti, R., Saso, L., Kukreti, S., 2019. Oxidative stress: a key modulator in neurodegenerative diseases. Molecules (Basel, Switzerland) 24, 1583. https://doi.org/10.3390/molecules24081583.

Solch, R.J., et al., 2022. Mediterranean diet adherence, gut microbiota, and Alzheimer's or Parkinson's disease risk: a systematic review. J. Neurol. Sci. 434, 120166. https://doi.org/10.1016/j.jns.2022.120166.

Stoeva, M.K., et al., 2021. Butyrate-producing human gut symbiont, Clostridium butyricum , and its role in health and disease. Gut Microbes 13. https://doi.org/10.1080/19490976.2021.1907272.

Su, M., et al., 2021. Butyric acid alleviated chronic intermittent hypoxia-induced lipid formation and inflammation through up-regulating HuR expression and inactivating AMPK pathways. Biosci. Rep. 41. https://doi.org/10.1042/BSR20203639.

Takiishi, T., Fenero, C., Camara, N., 2017. Intestinal barrier and gut microbiota: shaping our immune responses throughout life. Tissue Barriers 5, e1373208. https://doi.org/10.1080/21688370.2017.1373208.

Tanner, C.M., et al., 2011. Rotenone, paraquat, and Parkinson's disease. Environ. Health Perspect. 119, 866–872. https://doi.org/10.1289/ehp.1002839.

Thompson, T.B., Chaggar, P., Kuhl, E., Goriely, A., 2020. Protein-protein interactions in neurodegenerative diseases: a conspiracy theory. PLoS Comput. Biol. 16, e1008267. https://doi.org/10.1371/journal.pcbi.1008267.

VanLinden, M.R., Skoge, R.H., Ziegler, M., 2015. Discovery, metabolism and functions of NAD and NADP. Biochemist 37, 9–13. https://doi.org/10.1042/BIO03701009.

Vascellari, S., et al., 2020. Gut microbiota and metabolome alterations associated with Parkinson's disease. Msystems 5. https://doi.org/10.1128/mSystems.00561-20.

Wang, J., Sun, R., Xia, L., Zhu, X., Zhang, Q., Ye, Y., 2022. Potential therapeutic effects of NAMPT-mediated NAD biosynthesis in depression in vivo. Brain Sci. 12. https://doi.org/10.3390/brainsci12121699.

Weintraub, D., Aarsland, D., Chaudhuri, K.R., Dobkin, R.D., Leentjens, A.F., Rodriguez-Violante, M., Schrag, A., 2022. The neuropsychiatry of Parkinson's disease: advances and challenges. Lancet Neurol. 21, 89–102. https://doi.org/10.1016/S1474-4422(21)00330-6.

Xiao, J., et al., 2023. The mitochondrial-derived peptide (MOTS-c) interacted with Nrf2 to defend the antioxidant system to protect dopaminergic neurons against rotenone exposure. Mol. Neurobiol. 60, 5915–5930. https://doi.org/10.1007/s12035-023-03443-3.

Xue, L., et al., 2020. Fecal microbiota transplantation therapy for Parkinson's disease. Medicine 99, e22035. https://doi.org/10.1097/MD.0000000000022035.

Yemula, N., Dietrich, C., Dostal, V., Hornberger, M., 2021. Parkinson's disease and the gut: symptoms, nutrition, and microbiota. J. Parkinsons Dis. 11, 1491–1505. https://doi.org/10.3233/JPD-212707.

Yeung, A.W.K., et al., 2021. Reactive oxygen species and their impact in neurodegenerative diseases: literature landscape analysis. Antioxid. Redox. Sign. 34, 402–420. https://doi.org/10.1089/ars.2019.7952.

Zhang, Z.N., et al., 2017. Subcutaneous rotenone rat model of Parkinson's disease: dose exploration study. Brain Res. 1655, 104–113. https://doi.org/10.1016/j.brainres.2016.11.020.

Zhang, S., et al., 2023. Gut prevotellaceae-GABAergic septohippocampal pathway mediates spatial memory impairment in high-fat diet-fed ovariectomized mice. Neurobiol. Dis. 177, 105993. https://doi.org/10.1016/j.nbd.2023.105993.

Zhao, Z., Ning, J., Bao, X.Q., Shang, M., Ma, J., Li, G., Zhang, D., 2021. Fecal microbiota transplantation protects rotenone-induced Parkinson's disease mice via suppressing inflammation mediated by the lipopolysaccharide-TLR4 signaling pathway through the microbiota-gut-brain axis. Microbiome 9, 226. https://doi.org/10.1186/s40168-021-01107-9.

Zhou, Y., Zhen, Y., Wang, G., Liu, B., 2022. Deconvoluting the complexity of reactive oxygen species (ROS) in neurodegenerative diseases. Front. Neuroanat. 16, 910427. https://doi.org/10.3389/fnana.2022.910427.

Ziegler, M., Monné, M., Nikiforov, A., Agrimi, G., Heiland, I., Palmieri, F., 2021. Welcome to the family: identification of the NAD+ transporter of animal mitochondria as member of the solute carrier family SLC25. Biomolecules (Basel, Switzerland) 11, 880. https://doi.org/10.3390/biom11060880.

Zmora, N., Suez, J., Elinav, E., 2019. You are what you eat: diet, health and the gut microbiota. Nat. Rev. Gastroenterol Hepatol. 16, 35–56. https://doi.org/10.1038/s41575-018-0061-2.